Group theory of circular-polarization effects in chiral photonic crystals with four-fold rotation axes applied to the eight-fold intergrowth of gyroid nets

Matthias Saba,[1,*] Mark D. Turner,[2] Klaus Mecke,[1] Min Gu,[2] and Gerd E. Schröder-Turk[1,†]
[1]*Theoretische Physik, Friedrich-Alexander-Universität Erlangen-Nürnberg, 91058 Erlangen, Germany*
[2]*CUDOS & Centre for Micro-Photonics, Swinburne University of Technology, Victoria 3122, Australia*
(Received 9 August 2013; revised manuscript received 13 November 2013; published 11 December 2013)

We use group or representation theory and scattering matrix calculations to derive analytical results for the band structure topology and the scattering parameters, applicable to any chiral photonic crystal with body-centered-cubic symmetry $I432$ for circularly polarized incident light. We demonstrate in particular that all bands along the cubic [100] direction can be identified with the irreducible representations $E_{\pm}$, A, and B of the C_4 point group. E_+ and E_- modes represent the only transmission channels for plane waves with wave vector along the Δ line, and E_- and E_+ are identified as noninteracting transmission channels for right- and left-circularly polarized light, respectively. Scattering matrix calculations provide explicit relationships for the transmission and reflectance amplitudes through a finite slab which guarantee equal transmission rates for both polarizations and vanishing ellipticity below a critical frequency, yet allowing for finite rotation of the polarization plane. All results are verified numerically for the so-called **8-srs** geometry, consisting of eight interwoven equal-handed dielectric gyroid networks embedded in air. The combination of vanishing losses, vanishing ellipticity, near-perfect transmission, and optical activity comparable to that of metallic metamaterials makes this geometry an attractive design for nanofabricated photonic materials.

DOI: 10.1103/PhysRevB.88.245116 PACS number(s): 02.20.−a, 81.05.Xj, 33.55.+b, 42.70.Qs

Optical properties, such as optical rotation or circular dichroism, that are caused by a chiral structure of a light-transmitting medium or of its constituent molecules, remain of great interest in many different contexts. Circular dichroism spectroscopy of optically active molecules in solution is used in biochemistry where left-handed (LH) and right-handed (RH) molecular architectures cause different absorption properties for left-circularly polarized (LCP) and right-circularly polarized (RCP) light.[1] Optical activity of natural crystals such as quartz (see, e.g., Ref. 2) and of liquid crystals, both in the twisted nematic[3] and the blue phases,[4,5] is well known. Circularly polarized (CP) reflections of insect cuticles were observed by Michelson a century ago,[6] with circular-polarization effects an active topic in biophotonics of beetles,[7,8] crustaceans,[9,10] and butterflies,[11] and also the plant kingdom.[12] Nanofabrication technology nowadays allows for the fabrication of custom-designed chiral materials, both dielectric photonic crystals[13–15] and metallic metamaterials,[16–18] with the potential for technological photonic devices. This ability to fabricate custom-designed structures has led to noteworthy chiral-optical behavior, including strong circular dichroism,[19] negative refractive index[20] based on Pendry's prediction,[21] optically induced torque,[22] handedness switching in metamolecules,[23] and circular-polarized beam splitting.[15] Metallic or plasmonic metamaterials have been designed to give strong optical activity[16,18,24,25] that is orders of magnitudes stronger than in the natural materials.

This article makes a two-fold contribution to a deeper understanding of circular polarization effects in chiral materials. First, we combine group theory and scattering matrix treatment of chiral photonic crystals (PCs) to predict those properties of the band structure that are relevant for coupling to circularly polarized light. This analysis applies to *all* structures with cubic symmetry with at least one point that has 2-, 3-, and 4-fold point symmetry. Many of the ideas underlying this formalism are not specific to this symmetry group and apply, upon suitable adjustments, to structures with other symmetries. Second, we analyze in detail a specific chiral geometry that fulfils the symmetry requirements, namely the so-called **8-srs** structure consisting of eight interwoven non-overlapping gyroid (or **srs**) nets. Numerical data for its band structure and transmission coefficient, obtained by finite element simulations and finite-difference time-domain methods, are in perfect agreement with our theoretical predictions. Further, these simulations demonstrate that the **8-srs** geometry exhibits a particularly strong chiral-optical response. Specifically, in parts of the frequency spectrum, the lossless dielectric **8-srs** material with $\epsilon = 5.76$ is fully transparent for left- and right-circularly polarized (LCP and RCP) light, yet exhibits an optical activity that is comparable to metallic metamaterials. This suggests that the use of multiply intertwined gyroid nets, that can be realized with current nanofabrication methods, is promising for custom-designed photonic materials.

Polarization conversion measures the relative ratio of LCP to RCP light transmitted through a photonic material if the incident light was purely LCP. We will here use the term *optical activity* (OA) to denote the rotation of the polarization plane as a linearly polarized plane wave transmits through a chiral medium and *circular dichroism* (CD) is utilized to describe the difference in transmission rates for LCP and RCP light. The definition of OA and CD represent a slight deviation from the conventional nomenclature[27,28] where both refer to a respective phenomenological origin, i.e., a respective difference of the refractive indices and the absorption coefficients between LCP and RCP light.

Our use of these terms to describe differences in scattering parameters for CP light represents a natural adaption for a slab made of lossless but inhomogeneous material. With t and r denoting the scalar complex transmission and the reflection amplitudes, respectively, OA is the phase difference and CD is

the relative difference in absolute values between the complex scattering amplitudes $s_\pm \in \{t_\pm, r_\pm\}$ for an incoming left (LCP, $+$) or right (RCP, $-$) circularly polarized plane wave:

$$\mathrm{CD}_s = \frac{|s_+| - |s_-|}{|s_+| + |s_-|}, \quad \mathrm{OA}_s = \frac{\varphi_+^{(s)} - \varphi_-^{(s)}}{2}, \tag{1}$$

where the complex phase φ is given by the equation

$$e^{\imath\varphi_\pm^{(s)}} = \frac{s_\pm}{|s_\pm|}. \tag{2}$$

Group theoretic approaches to the optical properties of photonic crystals are motivated by the obvious importance of spatial symmetries in these systems. The common textbook example for this is the strict classification of discrete dispersion bands $\omega_n(\underline{k})$ of a two-dimensional PC into transverse-electric and transverse-magnetic modes if the wave vector $\underline{k}$ is restricted to the plane of periodicity.[29] In terms of circular polarization, the role of four-fold rotational symmetries, and more generally of $(m \geqslant 3)$-fold rotations, for the transmission and reflectance coefficients has been recognized.[30–38] In particular, it has recently been shown that any lossless structure with a 4-fold symmetry axis inclined perpendicular to this axis shows no circular dichroism and polarization conversion for normal incidence.[30] Our results on the scattering parameters for chiral PCs presented in this article are generalizations of previous works that derived related restrictions on reflection and transmission amplitudes for two-dimensional diffraction gratings made of quasiplanar particles[31–33,35] and also particles with 3D symmetry.[36,37] Group theory, or more precisely representation theory, is the natural language to deal with the influence of spatial symmetry on physical properties in general[39,40] and with photonic properties in particular.[40]

A particularly intricate design for a chiral photonic material is the so-called *single gyroid* (SG) or **srs** net,[41] with edges inflated to solid tubes with a given volume fraction ϕ. This periodic network is composed of identical three-coordinated nodes and has cubic chiral symmetry $I4_132$, without pure four-fold rotation axes;[42] the three-fold and four-fold screw axes correspond to three-fold and four-fold helical structures along the [111] and [100] directions, respectively. The theoretical prediction of circular dichroism for a dielectric photonic **srs** crystal[11] has been verified by nanofabrication experiments,[14,15] including also a **2-srs** structure[14] and an **srs** beamsplitter prism.[15] Recently, the first prediction of fully three-dimensional Weyl points has been published using photonic designs based on the SG.[43] For metallic **srs** nets, discrimination of LCP and RCP modes is observed,[44,45] but its magnitude is lower than what might be expected from its helical nature.[44] The relevance of the SG geometry, which is inspired by the biological PCs in wing scales of several butterflies,[46] as a chiral photonic material is increased by the ability to generate this structure at different length scales by molding from the self-assembly copolymer structure with unit cell size $a = 50$ nm,[47] replication of the butterfly structures with $a \approx 300$ nm,[48] direct laser writing with $a \gtrsim 1$ μm,[14,15] and cm-scale replica for microwave experiments.[49]

This article investigates a related geometry called **8-srs** consisting of eight identical equal-handed intertwined copies of the **srs** net.[50–52] As Fig. 1 demonstrates, the **8-srs** can be obtained by arranging translated copies of the **srs** net,

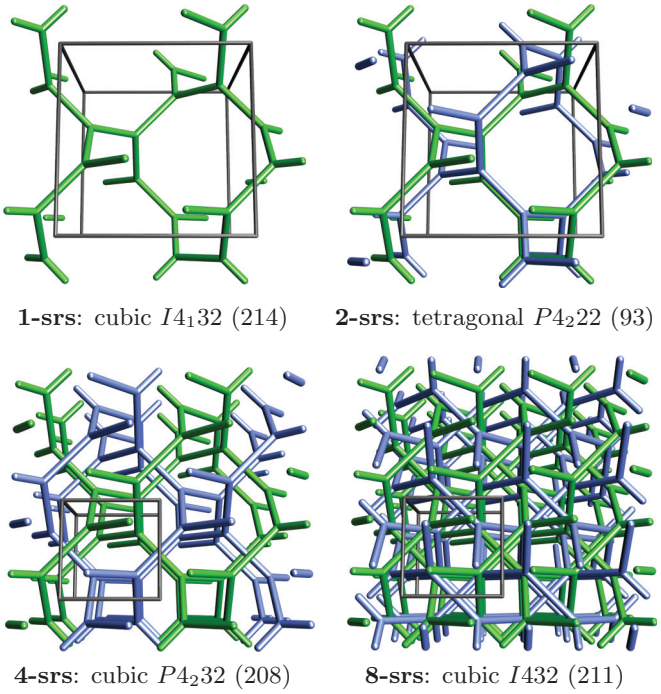

FIG. 1. (Color online) Construction of the **8-srs** by three replication steps. (a) **1-srs**: cubic $I4_132$ (214); (b) **2-srs**: tetragonal $P4_222$ (93); (c) **4-srs**: cubic $P4_232$ (208); (d) **8-srs**: cubic $I432$ (211). In each step the number of **srs** nets is doubled by generating translated copies (blue) of the already existing nets (green). All nets are identical and equal handed. Numbers in parentheses refer to the symmetry group numbers as in Ref. 26.

such that all 8 networks remain disjoint and to yield body-centered-cubic (BCC) symmetry $I432$; this is achieved by three orthogonal copy translations along the perpendicular [100] directions of the original **1-srs** net by $a = a_0/2$ where a_0 is the crystallographic lattice parameter of the **1-srs** in its space group $I4_132$. Figure 2 illustrates an alternative construction where the **8-srs** is obtained by the decoration of the hexagonal facets of a *Kelvin body*[53] by a degree-three network, such that 4-fold (square), 3-fold (triangle), and 2-fold (oval) rotations of

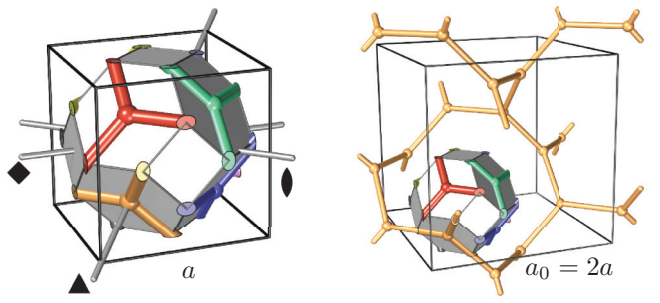

FIG. 2. (Color online) An alternative construction method that yields the same **8-srs** structure shown in Fig. 1. Left: The BCC translational unit cell is obtained by placing degree-three vertices at the midpoints of the hexagonal facets of a Kelvin body. Edges connect the hexagon's center point to every second vertex, such that rotational symmetries of the Kelvin body are maintained. Right: When repeated periodically, the **8-srs** consists of 8 equal-handed interwoven **srs** nets; only one of the eight nets is shown for clarity.

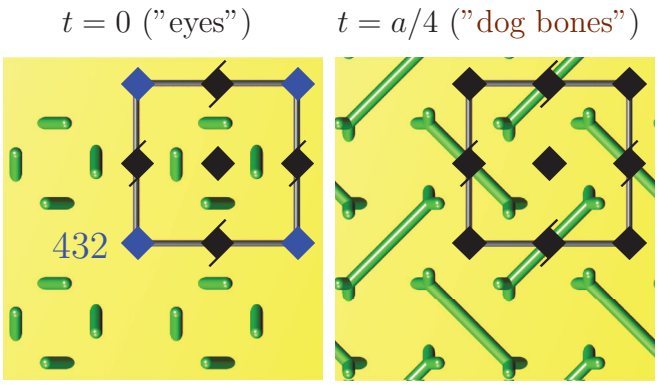

FIG. 3. (Color online) Different cross sections with [100] inclination through the **8-srs** reveal its four-fold symmetry. The parameter t denotes the position of the termination plane within the cubic unit cell. 4-fold rotation and 4_2 screw axes are marked by the square and barred square symbols, respectively. The gray square represents the cross section of the cubic unit cell whose vertices are located at the O (432) symmetry point marked by a blue square symbol (same choice as in Ref. 26).

the Kelvin body are maintained. This provides the BCC unit cell of the uncolored **8-srs** structures, with all components undistinguishable, whose lattice parameter a is half the size of the parameter a_0 of the individual **1-srs** nets. Note also the similar construction of the **8-srs** as an embedding on a Schwarz periodic primitive minimal surface in Fig. 12 of Ref. 52. In crystallographic notation, the **8-srs** has a single vertex at (1/4,1/4,1/4) at Wyckhoff site 8c (symmetry 32) and a single edge with midpoint (1/4,0,1/2) at Wyckhoff position 12d (symmetry 222), in the body-centered-cubic (BCC) space group $I432$ (No. 211 in Ref. 26) with lattice parameter $a = a_0/2$.[54] The **8-srs** has four-fold rotation axes *and* four-fold screw axes along the [100] lattice directions (see Fig. 3).

The spontaneous formation of the **8-srs** geometry by self-assembly is a long-term challenge, despite substantial recent progress in self-assembly of simpler polynetwork geometries.[55–58] However, the **8-srs** structure provides an immediately suitable design pattern for nanofabrication by direct laser writing technologies. Considering the realization of **1-srs** structures in low-dielectric polymers[14,15] and in high-dielectric chalcogenide glasses,[59] the fabrication of the **8-srs** material appears feasible.

This article is organized as follows: Section I introduces group theoretical concepts used in Sec. III to develop a treatment of band structure modes valid for any photonic crystal with symmetry group $I432$ (we henceforth refer to any such crystal as a $I432$ PC), including the **8-srs** geometry as a specific case, that can be readily extended to symmetries $P432$ or $F432$. This theory predicts the topology of the band structure at the Γ and H point and identifies LCP incident light with modes with irreducible representation E_-, and RCP with E_+. Numerical data for the band structure of the **8-srs** (Figs. 4 and 5) is in perfect agreement with these predictions, provided that the symmetry of the spatial grid is equally high as the structural symmetry; see Appendix B. A gap map providing the width and position of the band gap in the [100] direction as a function of dielectric contrast and volume fraction is provided

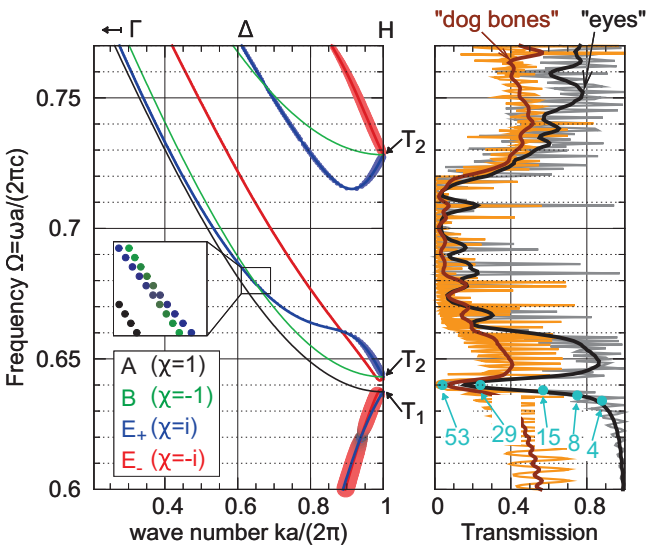

FIG. 4. (Color online) Photonic band structure and transmission spectrum of the **8-srs** PC. Left: Band structure for k along Δ (see Fig. 3). The bands are colored according to their symmetry behavior corresponding to the irreducible representations $i \in \{A, B, E_+, E_-\}$ of the C_4 point symmetry (cf. Table I). The $E_\pm$ bands that can couple to plane waves at normal incidence are further underlaid by dots of size proportional to the coupling constant β. Dots are smaller than the linewidth for $\beta \lessapprox 0.1$ and hence invisible. See discussion in Sec. III B for the meaning of the inset. Right: Transmission of light at normal incidence through a quasi-infinite slab of thickness $N_z = 53$, [100] inclination, and the two terminations shown in Fig. 3: $t = 0$ or the *eyes* cut shown in black and $T = 0.25a$ or the *dog bones* cut shown in brown. The spectrum is the same for any polarization state and is illustrated by the thin lines. The thick and more saturated lines represent a convolution with a Gaussian of width $\delta\Omega = 0.002$ eliminating the sharp Fano and Fabry-Pérot resonances. The teal points in the transmission spectrum mark the transmission minima at the *pseudo*–band gap at roughly $\Omega_g = 0.64$ for a slab of thickness $N_Z = 4, \ldots, 53$, respectively.

(Fig. 6). In particular, we analytically prove the following main statements in Sec. III:

Section III A: *Three-fold degeneracy at the H point*. The 4 lowest eigenstates at the H point are 3-fold degenerate. There are two T_1 and two T_2 modes (defined in Table I) and classified by their respective point symmetry behavior.[60]

Section III B: *Degeneracy fully lifted on* Δ. The degeneracy is fully lifted when going away from the high-symmetry points onto the Δ line. Each mode split is summarized by a compatibility relation $T_1 = A + E_+ + E_-$ or $T_2 = B + E_+ + E_-$ (Table I).

Section III C: *Inversion symmetry and slope at* Γ *and* H. Each band $\omega_i(k)$ along Δ is characterized by its *irreducible representation* $i \in \{A, B, E_+, E_-\}$. It has inversion symmetry $\omega_{A/B}(-\underline{k}) = \omega_{A/B}(\underline{k})$ and $\omega_{E_\pm}(-\underline{k}) = \omega_{E_\mp}(\underline{k})$. The bands $\omega_{A/B}(\underline{k})$ hence approach the points T_1 and T_2 with zero slope and the bands $\omega_{E_\pm}$ with slope of same magnitude but opposite sign.

Section III D: *The irreducible representations* $\{A, B, E_+, E_-\}$ *correspond to noninteracting scattering channels;* E_- *and* E_+ *represent RCP and LCP, respectively, and A and B are dark modes*. Modes of distinct representation

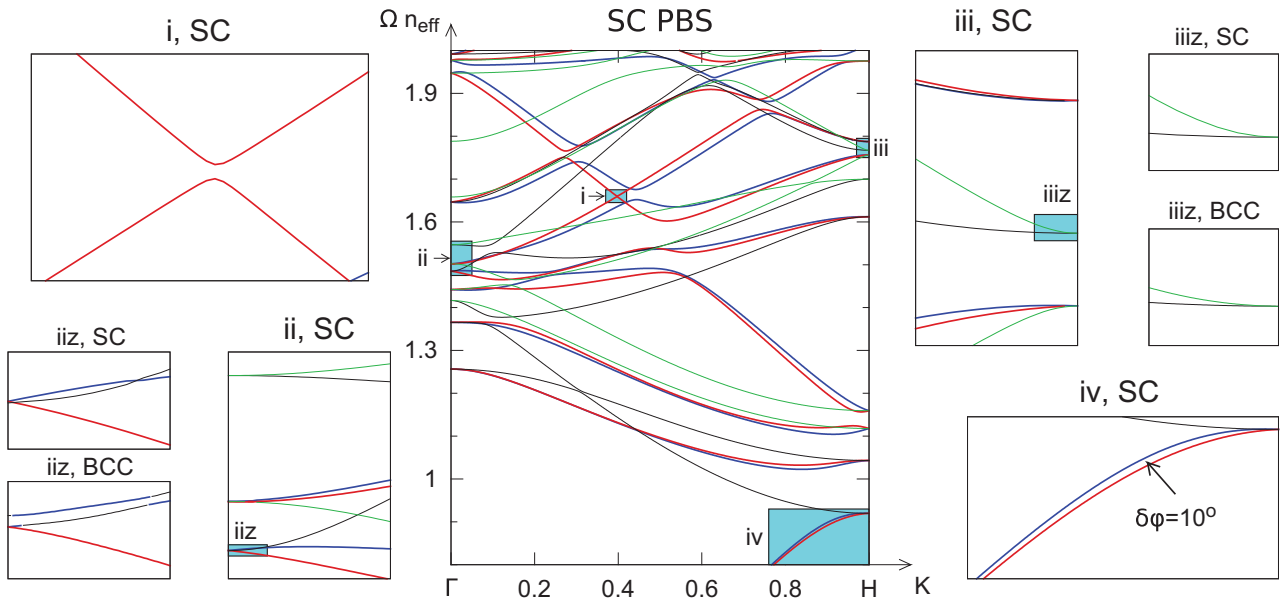

FIG. 5. (Color online) Band structure of the inverse **8-srs** PC for $\varepsilon = 1$ within the networks and $\varepsilon = 5.76$ outside and volume fraction $\Phi \approx 41\%$ (upper left quadrant in Fig. 6). The PBS is calculated using BCC and simple cubic (SC) symmetry. In the plots labeled "SC" the band structure of the simple cubic lattice is calculated for a grid discretization of $M^3 = 32^3$ and unfolded to the BCC Δ path (Ref. 73). The bands are colored by their respective symmetry behavior corresponding to $i = \{A, B, E_+, E_-\}$. Some of the interesting regions around H and Γ are magnified to demonstrate the excellent agreement between theory and numerics in the SC calculations. Plots labeled "BCC" use a BCC Fourier grid that does not maintain all symmetries of the BCC symmetry; see Appendix B. The BCC calculations illustrate that the violation of correct symmetry lifts the degeneracy of the bands at 3-fold degenerate points, even for a fine grid with $M = 64$.

do not interact. Scattering takes place in four independent channels characterized by the four representations A, B, E_+, E_-. For each channel, a well-defined scattering matrix relating the amplitudes of the outgoing plane waves to those of the incoming plane waves is found. Both A and B representations represent *dark* modes that do not couple to any plane wave at normal incidence. At normal incidence, any E_+ mode couples only to RCP and any E_- only to LCP plane waves. This implies that the channels corresponding to A and B do not contribute to the scattering process and there is no polarization conversion between LCP and RCP in transmission and reflection at any wavelength.

Section IV uses scattering matrix methods to provide analytical results for the scattering parameters, both for transmission and reflectance, that are valid for any structure with 4-fold symmetry that is inclined normal to its symmetry axis. The following two statements can be made:[61]

TABLE I. Character tables for the O and C_4 point groups relevant for the H (Γ) point and Δ line (Fig. 7), respectively. The time-reversal-symmetry type TR of the irreducible representations of C_4 are added in the last column (see Sec. III C).

O	$\mathbb{1}$	$6C_4$	$3C_2$	$8C_3$	$6C_2'$	C_4	$\mathbb{1}$	C_{4_1}	C_2	C_{4_3}	TR
A_1	1	1	1	1	1	A	1	1	1	1	(a)
A_2	1	−1	1	1	−1	B	1	−1	1	−1	(a)
E	2	0	2	−1	0	E_+	1	i	−1	$-i$	(b)
T_1	3	1	−1	0	−1	E_-	1	$-i$	−1	i	(b)
T_2	3	−1	−1	0	1						

Section IV C: *No CD and OA in reflectance*. The reflection matrices on both sides are identical for the E_+ (LCP) and the E_- (RCP) channel. For the reflection spectrum, CD and OA are hence strictly zero for all wavelengths.

Section IV D: *No CD in transmission below a critical frequency* Ω_c. The matrix norm of the transmission matrices is identical for E_+ and E_- channels. Henceforth, at low frequencies $\Omega := \omega a/2\pi c < \Omega_c := 1$, where the portion of energy that leaves the crystal in the (00) Bragg order $\Sigma_\pm = |t_\pm|^2 + |r_\pm|^2$ is strictly 100%, CD is zero. The matrix norm imposes no condition for circular dichroism above Ω_c. Optical activity may be finite at any frequency.

The predictions that OA and CD are always zero in reflection and that CD is zero below a threshold frequency in transmission are shown to be correctly reproduced by simulations of the **8-srs** (Fig. 9). The potential of the **8-srs** as a design for photonic materials, and in particular the magnitude of its optical activity relative to metallic metamaterials, is discussed in the conclusion section.

I. REPRESENTATION THEORY

A photonic band structure (PBS) can be seen as a classification of the eigenmodes of an infinite PC by their transformation behavior under its translational symmetry operations characterized by the Bloch wave vector $\underline{k}$. This classification yields a deeper understanding of the underlying physics and is also of practical use; the transverse dispersion for example yields a matching condition at interfaces. In this context, $\underline{k}$ acts as a continuous *quantum number*. Here, we additionally classify the band structure modes in the crystallographic [100]

direction by their transformation behavior under the PCs point symmetries (rotations, mirrors, etc.) and introduce a corresponding second discrete quantum number i.

The PBS eigenmodes are shown to belong to several orthogonal classes characterized by their symmetry transformation behavior. Group theory (or more specifically representation theory[39,40]) is used to show that there are four such classes with respect to the 4-fold rotation axis along the [100] direction that can be seen as noninteracting transmission channels. A circularly polarized and normally incident plane wave decomposes into one of the 4 symmetry classes alone and therefore couples light into the respective transmission channel only.

In the following, we use Dirac notation where the basis functions are denoted $|\alpha i\rangle$ and any operator acting on elements of the corresponding Hilbert space is marked with a hat. The basis functions are orthonormal; see theorem (iv) below. In this notation, a point group is a mathematical (in general non-Abelian) group with (unitary or length-preserving) point symmetry operations $\hat{R}$ as its elements and the operator $\cdot$ that is defined by the action onto any arbitrary function $|f\rangle$ via $(\hat{R}_1 \cdot \hat{R}_2)|f\rangle := \hat{R}_2(\hat{R}_1|f\rangle)$.

The operator $\hat{R}$ defines the operation of a point symmetry $R \in S$ where the point group S is a finite subgroup of the orthogonal group $O(3,\mathbb{R})$ for $I432$ and any other symmorphic space group. It can be represented by complex square matrices $\underline{\underline{D}}(R)$ so that the corresponding map is linear; i.e., $\underline{\underline{D}}(R_1 \cdot R_2) = \underline{\underline{D}}(R_2)\underline{\underline{D}}(R_1)$. A matrix representation $\underline{\underline{D}}(R)$ is called irreducible if no similarity transformation $\underline{\underline{D}}'(R) = \underline{\underline{D}}(R_0)\underline{\underline{D}}(R)\underline{\underline{D}}^{-1}(R_0)$ with $R_0 \in S$ exists that simultaneously transforms all $\underline{\underline{D}}(R)$ into the same block form; i.e., the representation cannot be split into representations of lower matrix dimension. Each representation has a set of basis functions $|\alpha\rangle$ for which the symmetry operator can be replaced by the representation matrix $\hat{R}|\alpha\rangle = \sum_\beta D_{\alpha\beta}(R)|\beta\rangle$, with α and β being *partners* of i and the corresponding indices denoting the rows and columns of $\underline{\underline{D}}$. In general, the matrices of an irreducible representation of dimension >1 and the corresponding basis functions are not unique due to similarity transformation gauge freedom. An irreducible representation i is uniquely characterized by the similarity transformation invariant trace of the respective matrix $\chi^{(i)}(R) = \sum_\alpha D^{(i)}_{\alpha\alpha}(R)$ that is also known as the character:[62]

$$(\forall R \in S : \chi^{(i)}(R) = \chi^{(j)}(R)) \quad \Leftrightarrow \quad i = j.$$

For our photonic mode analysis below we use four representation theorems that are all implications of the *Wonderful Orthogonality Theorem*[39] and the length-preserving nature of all point symmetry operations of $I432$:

(i) The eigenfunctions $|n\rangle$ of any operator $\hat{\vartheta}$ that commutes with all operations $\hat{R}$ of a point group S are generally given by the superposition of basis functions $|i\alpha\rangle$ of one irreducible representation i of S only:

$$(\forall \hat{R} \in S : [\hat{\vartheta}, \hat{R}] = 0) \quad \Rightarrow |n\rangle = \sum_\alpha c^{(i)}_\alpha |i\alpha\rangle := |n_i\rangle.$$

(ii) The characters of any arbitrary representation of a group S can be decomposed into the characters of the irreducible representations i by

$$\chi(R) = \sum_i d_i\, \chi^{(i)}(R) \quad \text{with} \quad d_i = \frac{1}{h}\sum_R \overline{\chi}^{(i)}(R)\chi(R),$$

where $\overline{z}$ denotes the complex conjugation of a complex number z and $h = \sum_R$ the number of symmetry operations in the point group.

(iii) Any arbitrary function $|f\rangle$ can be expressed by the complete set of basis functions $|i\alpha\rangle$ of the irreducible representations i:

$$|f\rangle = \sum_{i,\alpha} f^{(i)}_\alpha |i\alpha\rangle = \sum_{i,\alpha} \hat{P}^{(i)}_\alpha |f\rangle$$

with the operator $\hat{P}^{(i)}_\alpha$ that projects onto $|i\alpha\rangle$ given by

$$\hat{P}^{(i)}_\alpha = \frac{l_i}{h}\sum_R \overline{D}^{(i)}_{\alpha\alpha}(R)\hat{R},$$

where $l_i = \sum_\alpha$ is the dimension of the irreducible representation i.

(iv) The basis functions are orthogonal and can be normalized so that we assume for all representations i and j and partners α and β

$$\langle \alpha i|\beta j\rangle = \delta_{ij}\delta_{\alpha\beta}.$$

Representation theorem (i) is used to classify the band structure by the symmetry behavior. The magnetic wave

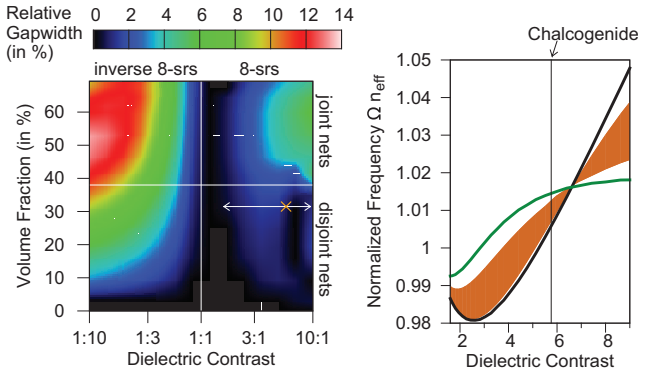

FIG. 6. (Color online) Relative gap width $\delta_G = 2(\omega_2 - \omega_1)/(\omega_2 + \omega_1)$ of the symmetry-induced band gap of midgap frequency Ω_G; ω_1 is the maximum frequency of the two fundamental bands of character E_+ and E_-, respectively, and ω_2 the minimum of the two air bands of the same character. Left: Color-coded map of δ_G as a function of volume fraction Φ and dielectric contrast $\psi = \varepsilon_{8-\mathrm{srs}} : \varepsilon_{\mathrm{background}}$ on a logarithmic scale. The join frequency $\Phi_J \approx 38\%$ indicates a topological change: For $\Phi < \Phi_J$, the individual **srs** nets are disconnected; for $\Phi > \Phi_J$ they overlap to form a single connected component. The orange point "x" marks the choice of parameters for Fig. 4. Right: Gap map along the line indicated by the white arrow on the left including the x point. The frequency is scaled by the effective index $n_{\mathrm{eff}} := \sqrt{\sum_m \Phi_m \varepsilon_m}$ with $m \in \{8-\mathrm{srs}, \mathrm{background}\}$ on the ordinate. The position of the band gap hence does not depend on the choice of the absolute value of dielectric constants. It turns out that the x point is close to a band structure topology change at $\Phi \approx 31\%$ and $\psi \approx 6.5$ where the T_1 (black curve) and T_2 (green curve) points at H are accidentally degenerate.

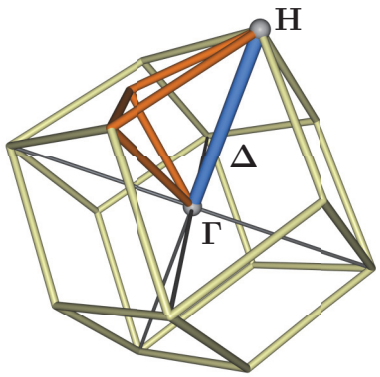

FIG. 7. (Color online) Brillouin zone of the BCC lattice: A rhombic dodecahedron whose edges are illustrated by yellow bars. The irreducible BZ (1/48 of the BZ due to 24 rotations in O (Table I) and another 24 time-inverted rotations) is the pyramid framed in orange. The Δ line marked in blue is one of its edges and connects the Γ point in the origin with the H point that is a 4-connected vertex of the BZ at $2\pi/a \cdot (1,0,0)^T$.

equation is given by

$$\vartheta_{\underline{k}}\underline{u}_{\underline{k}n}(\underline{r}) := (\imath\underline{k}+\underline{\nabla})\times\left[\frac{1}{\varepsilon(\underline{r})}(\imath\underline{k}+\underline{\nabla})\times\underline{u}_{\underline{k}n}(\underline{r})\right] = \frac{\omega_{\underline{k}n}^2}{c^2}\underline{u}_{\underline{k}n}(\underline{r})$$

with the periodic part of the Bloch field $\underline{u}_{\underline{k}n}(\underline{r})$, the periodic dielectric function $\varepsilon(\underline{r})$, the eigenfrequency $\omega_{\underline{k}n}$, the imaginary number $\imath := \sqrt{-1}$, and the velocity of light c. The operator[63] $\hat{\vartheta}_{\underline{k}}$ of a PC that has a given point symmetry S commutes with any symmetry element $\hat{R}$ that transforms the wave vector $\underline{k}$ into an equivalent wave vector $\underline{k}+\underline{G}$ that is translated by a reciprocal lattice vector $\underline{G}$ only (see Appendix A for a detailed proof of this statement). The set of all those operations $\hat{R}$ form a subgroup $S_{\underline{k}} \leqslant S$ and is called the group of the wave vector.

In our work we consider all modes of a bulk $I432$ PC that can couple to a normally incident plane wave at a (100) interface.[64] We choose a symmetric set of basis vectors $\underline{a}_1 = (-d,d,d)$, $\underline{a}_2 = (d,-d,d)$, $\underline{a}_3 = (d,d,-d)$, with $d = a/2$, for the body-centered-cubic translational symmetry. The Brillouin zone of the BCC lattice illustrated in Fig. 7 and the reciprocal lattice vectors are given by $\underline{b}_1 = (0,b,b)$, $\underline{b}_2 = (b,0,b)$, $\underline{b}_3 = (b,b,0)$, with $b = 2\pi/a$. All coupling modes[65] lie on a straight line within the Brillouin zone parametrized by $\underline{k}_s = s*(\underline{b}_2+\underline{b}_3-\underline{b}_1)$, $s \in (-0.5,0.5]$. The points at $s=0$ and $s=0.5$ are denoted by Γ and H, respectively. At both points, the group of the wave vector is equal to the full point group that together with the BCC translation gives the full $I432$ space group: That is the O (Schoenfliess)[66] point group that includes the point symmetries of a cube, i.e., 6 4-fold (C_4) and 3 2-fold (C_2) rotations around the [100] axes, 8 3-fold (C_3) rotations around the [111] axes, and 6 2-fold (C_2') rotations around the [110] axes (cf. Table I). On the Δ line that connects Γ and H [$s \in (0,0.5)$], the (Abelian) group of the wave vector is C_4, which only contains the 3 rotations around the [100] axis where positive (C_{4_1}) and negative (C_{4_3}) 4-fold rotations fall into distinct classes.[67]

II. PARAMETERS FOR NUMERICAL CALCULATIONS OF 8-srs PCs

A photonic crystal geometry with finite volume fraction is obtained by inflating all edges of the **8-srs** structure to solid cylindrical struts with permittivity ϵ, embedded in air or vacuum. For the quantitative results in Figs. 4 and 9 we assume a value $\epsilon = 5.76$, which closely resembles high-refractive-index chalcogenide glass at telecommunication wavelengths[68] or titanium dioxide at optical wavelengths;[48] the solid volume fraction is set to $\phi \approx 31\%$, corresponding to a rod diameter of $d \approx 0.115$; this value is well below the threshold where the distinct nets overlap to form a single connected component.[69,70] We consider in particular an infinitely wide slab of size $\infty \times \infty \times n_z a$ ($n_z = 4$ in Fig. 9 and $n_z = 53$ in Fig. 4),[71] with the crystallographic lattice vector [100] aligned with the z axis; all analyses are for wave vectors $\underline{k}$ along that axis. The two different terminations[72] illustrated in Fig. 3 for the **8-srs** crystal are chosen for the transmission simulation in Fig. 4.

III. TOPOLOGY AND SYMMETRY CLASSIFICATION OF THE BAND STRUCTURE

While the exact shape of the PBS strongly depends on geometry and dielectric contrast, the topology, i.e., degeneracies and hence also band connections at high-symmetry points, is generally induced by symmetry alone. This fact combined with symmetry-based selection rules is what makes group theory a powerful tool. Here, we derive the topology of the band structure of any $I432$ PC and show that, for the **8-srs** PC, these results are in perfect agreement with numerical results.

A. Degeneracies at the lowest Γ and H points

To derive the irreducible representation of the eigenmodes at the high-symmetry points in the BZ, it is suitable to group the plane wave components $\underline{u}_{\underline{G}\sigma}(\underline{r}) = \underline{u}_{\underline{G}\sigma}e^{\imath(\underline{k}+\underline{G})\cdot\underline{r}}$ of a Bloch mode $\underline{u}_{\underline{k}n_i}(\underline{r}) = \sum_{\underline{G}\sigma}\underline{u}_{\underline{G}\sigma}(\underline{r})$ with $\sigma \in u,v$ denoting a linear polarization basis by the length of $\underline{k}+\underline{G}$, i.e., its vacuum frequency, in equivalence classes $[\underline{k}+\underline{G}] := \{\underline{u}_{\underline{G}\sigma}\underline{G}' : |\underline{k}+\underline{G}| = |\underline{k}+\underline{G}'|\}$. We sort the equivalence classes at the high-symmetry points by ascending vacuum frequency and denote the corresponding class by $\Gamma^{(n)}$ and $H^{(n)}$ ($n \in \mathbb{N}_0$), respectively. All elements within each equivalence class form a basis for a (generally reducible) representation of the group of the wave vector $\underline{k}$ by its definition. This representation can then be reduced into irreducible representations of the group of the wave vector with representation theorem (ii).

We first consider the $H^{(0)}$ point with $|\underline{k}+\underline{G}| = b$. There are 6 points in the group of the wave vector with $\underline{k} = \pm b\underline{e}_i$ ($i \in x,y,z$). Hence, there are 12 plane waves that form a closed set of basis functions for a reducible representation $\mathcal{R}(H^{(0)})$ within the O point group. The character of this reducible representation is determined by the corresponding representation matrix of a point symmetry R. First, we need to know how many of these points are unchanged under R as we only count diagonal elements to obtain the trace, i.e., equivalent to the number of points on the axis (or plane) of symmetry. Then we multiply by the character of the point symmetry acting on a two-dimensional vector in the plane

perpendicular to the axis of symmetry which is the contribution of the polarization mode pair on each point: The character of the identity transformation $\mathbb{1}$ is 2, of the C_4 rotation 0 and of the C_2 rotation -2. All other operations change all $\underline{k}$ on the H_n or Γ_n points into $\underline{k}+\underline{G}$ with $\underline{G}\neq 0$ and hence cannot contribute to the trace. The described procedure yields the following characters:

R	$\mathbb{1}$	$6C_4$	$3C_2$	$8C_3$	$6C_2'$
$\chi_{\mathcal{R}(H^{(0)})}(R)$	12	0	-12	0	0

Note that the number -12 for the C_2 rotation already includes the number of elements in that class, i.e., 3. Applying representation theorem (ii) using the characters in Table I we obtain the *compatibility relation* $\mathcal{R}=2T_1+2T_2$ that tells us that the 12-dimensional representation of the plane waves at the high-symmetry points is reduced into respectively 2 three-dimensional representations T_1 and T_2 that are irreducible within O. This result is also numerically obtained and illustrated in Fig. 4.

Analogously, the irreducible representations for all higher order $\Gamma^{(n)}$ and $H^{(n)}$ points can be obtained. For example, $\Gamma^{(1)}=[(b,b,0)^T]$ has 24 elements yielding the reducible representation with the following characters:

R	$\mathbb{1}$	$6C_4$	$3C_2$	$8C_3$	$6C_2'$
$\chi_{\mathcal{R}(\Gamma^{(1)})}(R)$	24	0	0	0	-24

and the compatibility relation $\mathcal{R}(\Gamma^{(1)})=2A_2+2E+4T_1+2T_2$. $H^{(1)}=[(b,b,b)^T]$ has 16 elements on a C_3 axis. The compatibility relation is $\mathcal{R}(H^{(1)})=2E+2T_1+2T_2$. These results are summarized in Table II.

B. Degeneracy fully lifted on the Δ line

Instead of also reducing an equivalent representation to $\mathcal{R}$ on the respective Δ line we reduce the irreducible representations of O in the C_4 point group to learn how the degeneracies are lifted when going away from the high-symmetry points onto Δ. The characters are

R	$\mathbb{1}$	C_{4_1}	C_2	C_{4_3}
$\chi_{A_1}(R)$	1	1	1	1
$\chi_{A_2}(R)$	1	-1	1	-1
$\chi_{E}(R)$	2	0	2	0
$\chi_{T_1}(R)$	3	1	-1	1
$\chi_{T_2}(R)$	3	-1	-1	-1

The same reduction procedure as above yields the compatibility relations listed in Table III. The degeneracy is in each case completely lifted as all the irreducible representations of C_4 are one-dimensional (cf. Table I).

For the **8-srs** PC, the modes perfectly match in the predicted manner in numerical calculations if the Fourier lattice maintains the full O symmetry (Fig. 5). The eigenmodes of the band structure in Fig. 4 that are colored by their respective C_4 irreducible representation show the predicted behavior. Each mode representation is obtained numerically by projecting the corresponding normalized magnetic field $|\underline{H}\rangle$ onto the respective basis function with representation theorem (iii). The representation is determined with the norm $N_i=\sum_\alpha\langle\hat{P}^{(i)}_\alpha\underline{H}|\hat{P}^{(i)}_\alpha\underline{H}\rangle$ (see also Ref. 74) of each projection onto one of the 4 one-dimensional irreducible representations. Up to numerical accuracy, the projection onto the true irreducible representation yields $N_i=1$ while all other projections vanish if a simple cubic lattice with full O symmetry is used (cf. Appendix B) for the MPB calculations of the PBS; see Fig. 5.

TABLE II. Summary of the results of Sec. III A. The vacuum frequency Ω_0, a representative wave vector, and the compatibility relation are respectively listed for the 4 lowest points where the group of the wave vector exhibits O symmetry. We use a dagger (†) at the T_1 representation for $\Gamma^{(0)}$ to indicate that the T_1 representation does not split into $A+E_+ +E_-$ but only into $E_+ +E_-$. The static A mode exists at $\Gamma^{(0)}$ itself to give a full basis for a homogeneous 3D vector field. However, it violates the divergence theorem for $k\gtrapprox 0$.

$[\underline{k}]$	Ω_0	$\underline{k}$	$\mathcal{R}=$
$\Gamma^{(0)}$	0	$(0,0,0)^T$	$T_1^\dagger$
$H^{(0)}$	1	$(b,0,0)^T$	$2T_1+2T_2$
$\Gamma^{(1)}$	$\sqrt{2}$	$(b,b,0)^T$	$2A_2+2E+4T_1+2T_2$
$H^{(1)}$	$\sqrt{3}$	$(b,b,b)^T$	$2E+2T_1+2T_2$

The Maxwell version of the Hellmann-Feynman theorem, i.e., $(d/d\lambda)\langle\underline{H}|\hat{\vartheta}\underline{H}\rangle=\langle\underline{H}|(d\hat{\vartheta}/d\lambda)\underline{H}\rangle$ for any parameter λ, yields directly that the band function $\omega_{ni}(\underline{k})$ is continuously differentiable and has a slope given by the average energy flow of the corresponding eigenmode which can be shown to be always less than the velocity of light c.[75] Orthogonality of the irreducible representations further implies that the function $\underline{H}_{ni\underline{k}}(\underline{r})$ does not change its representation i if the $\underline{k}$ vector does not change its point symmetry behavior under the transformation $\underline{k}\to\underline{k}+\delta\underline{k}$. The argument also holds at accidental degeneracies where the different representations are still orthogonal and usually even at symmetry-triggered degeneracies.[76] Bands can therefore either cross (A and B band in the lower half of Fig. 5 "ii, SC") or *anticross* (two red bands in Fig. 5 "i, SC").[77]

C. Time-inversion symmetry and slope at Γ and *H*

Due to time-reversal symmetry it is sufficient to show the band structure along the Δ line (including Γ and H). To obtain the mode representations of the other half we examine the action of the time-reversal operator $\hat{T}$ on the modes and eigenfrequencies. $\hat{T}$ is defined by $\hat{T}f(t)=f(-t)$. The action on the (complex) spatial part $f(\underline{r})$ of a monochromatic field $f(\underline{r},t)=\mathrm{Re}\{f(\underline{r})\exp(-\imath\omega t)\}$ is then given by the antiunitary complex conjugation operator, i.e., $\hat{T}f(\underline{r})=\overline{f}(\underline{r})$, that obeys

TABLE III. Compatibility relations obtained by reduction of the irreducible representations of O in C_4.

$\mathcal{R}(O)$	A_1	A_2	E	T_1	T_2
$\mathcal{R}(C_4)$	A	B	$A+B$	$A+E_+ +E_-$	$B+E_+ +E_-$

$\hat{T}^2 = \hat{E}$ and transforms the Bloch-Maxwell operator into one with opposite wave vector:

$$\hat{\vartheta}'_{\underline{k}} = \hat{T}\hat{\vartheta}_{\underline{k}}\hat{T}^{-1} = \hat{T}\hat{\vartheta}_{\underline{k}}\hat{T} = \hat{\vartheta}_{-\underline{k}}.$$

The action on an eigenfunction $|\underline{k}i\rangle$ characterized by its wave vector $\underline{k}$ and representation i is generally given by

$$\hat{T}|\underline{k}i\rangle = |-\underline{k},i'\rangle.$$

The positive-definite[29] nature of $\hat{\vartheta}_{\underline{k}}$ yields the frequency "degeneracy" $\omega_i(\underline{k}) = \omega_{i'}(-\underline{k})$.[78] We distinguish two cases[79] (cf. Refs. 39 and 80):

(a) $\exists R' \in G : \forall R \in G$

$$\overline{\underline{\underline{D}}(R')\,\underline{\underline{D}}(R)\,\underline{\underline{D}}(R')^{-1}} = \underline{\underline{D}}(R')\,\underline{\underline{D}}(R)\,\underline{\underline{D}}(R')^{-1},$$

(b) $\nexists R' \in G : \forall R \in G$

$$\overline{\underline{\underline{D}}}_i(R) = \underline{\underline{D}}(R')\,\underline{\underline{D}}_i(R)\,\underline{\underline{D}}(R')^{-1}.$$

As time inversion $\hat{T}$ commutes with the point symmetry operations $\hat{R}$, i' is equal to i in case (a). As a proof for that statement we choose the representation whose matrix entries are all real so that the time-reversal state transforms as a state of irreducible representation i:

$$\begin{aligned}\hat{R}|-\underline{k}i'\alpha\rangle = \hat{R}\hat{T}|\underline{k}i\alpha\rangle &= \sum_\beta \hat{T}\,\underline{\underline{D}}^{(i)}_{\alpha\beta}(R)|\underline{k}i\beta\rangle \\ &\overset{(a)}{=} \sum_\beta \underline{\underline{D}}^{(i)}_{\alpha\beta}(R)\hat{T}|\underline{k}i\beta\rangle \\ &= \sum_\beta \underline{\underline{D}}^{(i)}_{\alpha\beta}(R)|-\underline{k}i'\beta\rangle.\end{aligned}$$

Contrarily, i and i' are different irreducible representations (of the same dimension) in case (b) that form a *quasidegenerate* pair so that

$$\begin{aligned}\omega_i^2(\underline{k})/c^2 &= \langle\underline{k}i|\hat{\vartheta}_{\underline{k}}\underline{k}i\rangle = \langle\hat{T}^2\underline{k}i|\hat{\vartheta}_{\underline{k}}\hat{T}^2\underline{k}i\rangle \\ &= \langle(\hat{T}\hat{\vartheta}_{\underline{k}}\hat{T})\hat{T}\underline{k}i|\hat{T}\underline{k}i\rangle = \langle\hat{\vartheta}_{-\underline{k}} - \underline{k},i'|-\underline{k},i'\rangle \\ &= \omega_{i'}^2(-\underline{k})/c^2.\end{aligned}$$

This quasidegenerate pair naturally meets at both the Γ and the H point. The respective case for each irreducible representation can be determined by the Herring rules.[81] The pair of two-fold rotations in O perpendicular to the [100] direction is responsible for a nontrivial behavior along Δ. The different cases are listed in Table I. At the Γ and the H point, the irreducible representations of O are all of time-inversion type (a).

In accordance with the compatibility relations above, a pair of E_+ and E_- modes along Δ hence always meets at the H (Γ) point. Their group velocity in the vicinity is further of same magnitude and opposite sign. The A and B representations on the other hand always have vanishing group velocity close to Γ and H.

D. $\{A, B, E_+, E_-\}$ correspond to noninteracting scattering channels

The mode structure of the C_4 representations is strongly connected to a plane wave propagating along the axis of symmetry. We derive the symmetry behavior of such a plane wave using a circular polarization basis; i.e., we make use of representations theorem (iii) to calculate the composition of an RCP/LCP wave. The modulation factor $\exp\{\imath kz\}$ is obviously unchanged by any operation within C_4 so that $\hat{R}$ is only acting on the Jones vector for which we obtain

$$\begin{aligned}\begin{pmatrix}1\\ \mp\imath\\ 0\end{pmatrix} &= \sum_i \frac{l_i}{h}\sum_{R\in C_4}\chi_i(R)\hat{R}\begin{pmatrix}1\\ \mp\imath\\ 0\end{pmatrix} \\ &= \sum_i \frac{1}{4}\left\{\chi_i(\mathbb{1})\begin{pmatrix}1\\ \mp\imath\\ 0\end{pmatrix} + \chi_i(C_{4_1})\begin{pmatrix}\pm\imath\\ 1\\ 0\end{pmatrix}\right. \\ &\quad \left. + \chi_i(C_2)\begin{pmatrix}-1\\ \pm\imath\\ 0\end{pmatrix} + \chi_i(C_{4_3})\begin{pmatrix}\mp\imath\\ -1\\ 0\end{pmatrix}\right\} \\ &= \begin{cases}\begin{pmatrix}1\\ \mp\imath\\ 0\end{pmatrix}, & \text{if} \quad i = E_\mp, \\ 0, & \text{else.}\end{cases}\end{aligned}$$

Therefore, any LCP/RCP mode transforms purely according to the irreducible representation $E_\pm$, respectively; there is strictly no contribution of an A or B representation to any plane wave traveling along a C_4 axis. As a result, the two distinct circular polarization states scatter in orthogonal and hence independent channels corresponding to $E_\pm$ because of representation theorem (iv). Polarization conversion vanishes for any scattering process at a 4-fold symmetric structure.

While the rigorous proof is provided above, an intuitive understanding is easily obtained by going the reverse logical way starting from the four irreducible representations and calculating the coupling strength with a plane wave. This idea is illustrated in Fig. 8.

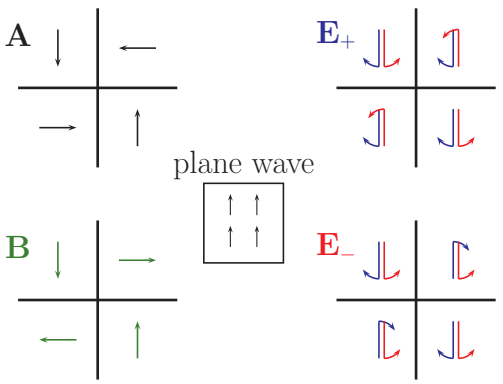

FIG. 8. (Color online) Illustration of the four mode structures of a monochromatic vector field that spatially transform according to the respective irreducible representation of C_4 (cf. Table I). The field is shown at an arbitrary point in time at four symmetry-equivalent points. For the $E_\pm$ modes for which the characters are not all real, the transformation depends on the polarization state and we split each mode into a red RCP part with temporally right rotation as seen from the receiver and a blue LCP part rotating opposite. The A and B profiles do not couple to a plane wave (center) as opposite contributions with a phase shift of π cancel out. The RCP part of an E_+ mode and the LCP part of an E_- mode cannot couple to a plane wave for the same reason.

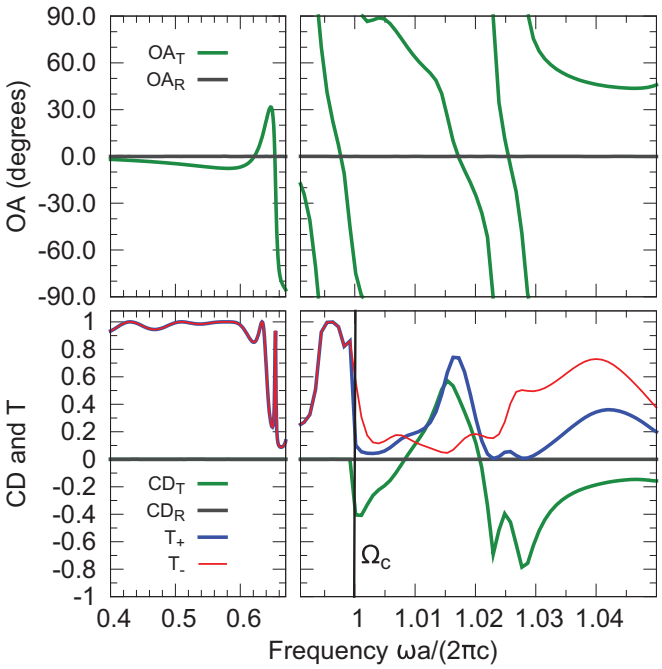

FIG. 9. (Color online) Simulated circular dichroism (CD) and optical activity (OA), defined in Eq. (1), and transmissivity $T_\pm$ in both transmission channels $E_\pm$ for the reflection and transmission of a plane wave at normal incidence: The **8-srs** PC slab has termination $t = 0.25a$ and thickness $N_z = 4$. Since optical experiments cannot measure phase differences $>\pm 90°$, OA is wrapped onto the interval $[-90°,90°]$ by OA $\mapsto$ arctan[tan(OA)].

We finally note that time inversion exchanges the representations $E_\pm$ that are defined respective to a static Cartesian coordinate system whereas it leaves the circular polarization state unchanged. (Note that is defined respective to a right-handed coordinate system depending on the propagation direction $\underline{k}$ that changes its sign under time-inversion symmetry.)

IV. GENERAL PREDICTIONS FOR SCATTERING PARAMETERS

General features of the scattering matrix for a finite slab of an $I432$ PC with (100) inclination can be derived by its 4-fold symmetry alone. In the following, no energy dissipation in any of the PC materials is assumed. Kaschke *et al.* recently calculated in Ref. 30 that there is no circular dichroism in the reflectance and transmittance for any lossless structure if any higher order scattering is neglected. Here, we show more precisely that the reflectivity matrix of the same system is identical for RCP and LCP light at all frequencies; i.e., circular dichroism and optical activity are zero. In the transmission spectrum, optical activity is present and particularly strong above the fundamental bands whereas circular dichroism is zero at frequencies below $\Omega_c = 1$. Above the critical frequency Ω_c, the (10) Bragg order becomes leaky so that transmission + reflection = 1 is no longer a valid statement if both are just measured within the (00) Bragg order (Fig. 9).

A. Introduction of a well-defined scattering matrix

We first show that a scattering matrix for any photonic crystal slab with 4-fold symmetry normal to its clipping planes can be well defined. We use representation theorem (iii) to define a set of symmetry-adapted Floquet basis functions of the in-plane vector $\underline{r} = (x,y)^T$ that transform according to the irreducible representations of the C_4 point group:

$$|(\underline{n}\sigma)i\rangle \equiv f^{(i)}_{\sigma,\underline{n}}(\underline{r}) = \frac{1}{2}\sum_{R\in C_4} \overline{\chi}_i(R)\hat{R}\,\underline{e}_\sigma e^{\imath \underline{G}_{\underline{n}}\cdot\underline{r}}.$$

Those basis functions are characterized by their irreducible representation $i \in \{A,B,E_+,E_-\}$ (Table I), polarization $\sigma \in \{s,p\}$, and a corresponding unit vector e_σ[82] and Bragg order $\underline{n} = (n_1,n_2)$ (with $n_1 \in \mathbb{N}_1$ and $n_2 \in \mathbb{N}_0$) that defines the reciprocal grating vector $\underline{G}_{\underline{n}} = (2\pi/a)\underline{n}$. To obtain a complete set for the normal incidence scattering problem, only two additional (00) Bragg order basis functions $f^{E_\pm}_{x,(0,0)^T}(\underline{r})$ are added to the above.[83] The symmetry-adapted basis functions are easily shown to be plane orthogonal using the orthogonality of plane waves, the Cartesian basis vectors, and the Wonderful Orthogonality Theorem of representation theory:

$$\frac{1}{a^2}\int_{-a/2}^{a/2} dx \int_{-a/2}^{a/2} dy\, \overline{f}^{(i)}_{\sigma,\underline{n}} f^{(i')}_{\sigma',\underline{n}'} = \delta_{i,i'}\delta_{\sigma,\sigma'}\delta_{\underline{n},\underline{n}'}.$$

We use the compact Dirac notation so that the electromagnetic fields $|F_{(\underline{n}\sigma)i}\rangle$ in vacuum that are involved in the scattering process are expressed by

$$|F_{(\underline{n}\sigma)i}\rangle := \begin{pmatrix} |E_{(\underline{n}\sigma)i}\rangle \\ |H_{(\underline{n}\sigma)i}\rangle \end{pmatrix} = \begin{pmatrix} 1 \\ H_{(\underline{n}\sigma)i,q_d} \end{pmatrix} |(\underline{n}\sigma)i\rangle \otimes |q_d\rangle,$$

where $d = \pm$ denotes the sign ambiguity for $|q_d\rangle \equiv e^{\imath q_d z}$ with $q_d = d\sqrt{\omega^2/c^2 - |\underline{G}_{\underline{n}}|^2}$ defined by the vacuum dispersion relation. The Bloch fields within a thin layer[84] of thickness δ also transform as one irreducible representation i only and are hence given by

$$|\mathcal{F}_{\alpha i}\rangle = \begin{pmatrix} |\mathcal{E}_{\alpha i}\rangle \\ |\mathcal{H}_{\alpha i}\rangle \end{pmatrix} = \sum_{\underline{n}\sigma} \begin{pmatrix} \mathcal{E}^{(\alpha)}_{(\underline{n}\sigma)i,q_d} \\ \mathcal{H}^{(\alpha)}_{(\underline{n}\sigma)i,q_d} \end{pmatrix} |(\underline{n}\sigma)i\rangle \otimes |q_d\rangle,$$

where within the layer $|q_d\rangle \equiv e^{\imath q_d z}$ is again a plane wave whose wave vector q_d however has no analytical expression[85] and d is hence chosen by $\mathrm{sgn}(\mathrm{Im}\{q\})$ if $\mathrm{Im}\{q\} \neq 0$ and $\mathrm{sgn}(\mathrm{Re}\{q\})$ else.[86] Because of the orthogonality $\langle ai|bj\rangle = \delta_{ab}\delta_{ij}$ a scattering matrix treatment within each channel i analogous to the calculation described by Whittaker and Culshaw[87] can be performed and (with $\delta \to 0$) yields a well-defined scattering matrix for the whole structure that relates the (generally countably infinite number of) amplitudes $c^{(a)}_{O\,\mu}$ of the outgoing symmetry-adapted Floquet waves to the amplitudes $c^{(a)}_{I\,\mu}$ of the corresponding incoming waves; $\mu = 1$ and $\mu = 2$ indicate the lower ($z_{\min}$) and upper ($z_{\max}$) surface of the slab, respectively. Outgoing waves are defined as those with positive d at surface 1 and negative d at surface 2 (and vice versa for incoming waves). With a vector $\underline{c}$ going over all indices a, the scattering matrix $\underline{\underline{S}}$ is defined within each 4-fold channel $i \in \{A,B,E_+,E_-\}$ by

$$\begin{pmatrix} \underline{c}_{O1} \\ \underline{c}_{O2} \end{pmatrix} = \begin{pmatrix} \underline{\underline{S}}_{11} & \underline{\underline{S}}_{12} \\ \underline{\underline{S}}_{21} & \underline{\underline{S}}_{22} \end{pmatrix} \begin{pmatrix} \underline{c}_{I1} \\ \underline{c}_{I2} \end{pmatrix}.$$

The definition of q_d implies that nonzero entries in $\underline{c}_{I\,1/2}$ are only physical for $\Omega \geqslant |\underline{n}|$, such that the corresponding

fields are propagating. The same condition applies for all entries in $\underline{c}_{O\,1/2}$ that contribute to the far field. Further, if the incoming field is at normal incidence only the 4-fold channels that transform as $E_\pm$ are relevant as shown above with the LCP/RCP Jones vectors. We therefore restrict further arguments to the square submatrices $\underline{\underline{S}}_\pm$ that relate the propagating Floquet modes in the respective scattering channel corresponding to $E_\pm$.

B. General properties of the scattering matrix

We now prove by energy conservation and time-inversion symmetry that the reflectance spectrum (in the far field) is exactly the same for RCP and LCP incident light whereas the transmittance spectrum has different phases for all frequencies and different magnitudes if $\Omega \geqslant 1$. These predictions are precisely reproduced for the **8-srs** by a numerical calculation in Fig. 9.

In scattering theory, the scattering matrix is often assumed to be unitary. We prove that this is also true for the particular problem. Averaging Poynting's theorem over time for the monochromatic fields yields the spatially local equation $\underline{\nabla} \cdot \mathrm{Re}\{\underline{\overline{E}} \times \underline{H}\} = 0$. We integrate this equation over a box of size $a \times a \times l$ that is centered around the photonic crystal slab with $l \to \infty$. Because of the mode structure of the 4-fold modes the parallel components of the Poynting vector vanish at each point so that the divergence theorem yields the equation $\mathrm{Re}\{\int_A \underline{\overline{E}}_\parallel \times \underline{H}_\parallel\} = 0$ where only the propagating fields parallel to the surface are integrated over the top and bottom $a \times a$ surfaces.

The orthogonality of the basis functions when averaged yields that all mixed contributions in different Bragg orders vanish. We show that for interface 2 and s polarization (p polarization is analogously done) the electric field only has the following ϕ component:

$$E_\phi = \frac{1}{2}[c_O e^{\imath qz} + c_I e^{-\imath qz}] \sum_R \overline{\chi}_i(R) e^{\imath \underline{\underline{G}}_R \cdot \underline{r}}.$$

Since the z component of the magnetic field is irrelevant here we only calculate the in-plane field that is purely radial and obtained by Faraday's law:

$$H_r = \frac{\imath c}{2\omega}\partial_z E_\phi = \frac{-cq}{2\omega}[c_O e^{\imath qz} - c_I e^{-\imath qz}] \sum_R \overline{\chi}_i(R) e^{\imath \underline{\underline{G}}_R \cdot \underline{r}}.$$

The left side of the integrated Poynting's theorem for s polarization is therefore given by

$$\begin{aligned} -\mathrm{Re}\left\{ \int_A \overline{E}_\phi \, H_r \right\} &= \mathrm{Re}\left\{ \frac{cqa^2}{4\omega}[\overline{c}_O e^{-\imath qz} + \overline{c}_I e^{\imath qz}] \right. \\ &\qquad \left. \times [c_O e^{\imath qz} - c_I e^{-\imath qz}] \sum_R |\chi_i(R)|^2 \right\} \\ &= \frac{cqa^2}{\omega}[|c_O|^2 - |c_I|^2]. \end{aligned}$$

The purely imaginary cross-correlated contributions vanish (i.e., they average out over time as intuitively expected). The same result is obtained for surface 1 so that for $q > 0$ Poynting's theorem yields for each Bragg order in each 4-fold channel

$$|\underline{c}_{O1}|^2 + \left|\underline{c}^{(a)}_{02}\right|^2 = \left|\underline{c}^{(a)}_{I1}\right|^2 + \left|\underline{c}^{(a)}_{I2}\right|^2.$$

The scattering matrix is hence norm preserving and therefore unitary by Wigner's theorem.

A correlation between the scattering matrices in different channels can be derived by time-inversion invariance. We act with $\hat{T}$ upon the equation that defines the scattering matrix and note that the vectors satisfy $\overline{\underline{c}}_{I\pm}(E_+) = \underline{c}_{O\pm}(E_-)$ (and also with I and O exchanged) because the basis functions $|ai\rangle$ stay unchanged by the complex conjugation except for a change in representation $\chi_{E_\pm}(R) \to \overline{\chi}_{E_\pm}(R) = \chi_{E_\mp}(R)$[88] whereas the function of z changes its sign $\hat{T}|q_+\rangle = |q_-\rangle$. The complex conjugated scattering matrix in one channel is hence the inverse of the matrix in the other channel; i.e., $\underline{\underline{\overline{S}}}_\pm = \underline{\underline{S}}^{-1}_\mp$.

C. No CD and OA in reflectance

We combine both results and identify the diagonal entries $\underline{\underline{S}}_{ii}$ with the reflection matrices on either side to obtain $\underline{\underline{R}}^{(+)} = \underline{\underline{R}}^{(-)}$; i.e., the reflection matrices are identical and hence OA and CD vanish to any numerical precision for all frequencies (cf. Fig. 9). We present an illustrative interpretation of this result in Fig. 10 based on the assumption that there is only a single mode per channel and propagation direction. If the assumptions made in Fig. 10 are met (as is for example the case for the two fundamental bands), the Airy formula in terms of the interfacial scattering parameters defined in Fig. 10 yields for the transmission and reflection amplitudes with $p^{\uparrow\downarrow}_\pm := \exp\{\varphi^{\uparrow\downarrow}_\pm\}$

$$\begin{aligned} t &= t^{\uparrow,L}_\pm p^{\uparrow}_\pm t^{\uparrow,U}_\pm \sum_{n=0}^{\infty} (r^{\uparrow\downarrow,U}_\pm p^{\downarrow}_\pm r^{\downarrow\uparrow,L}_\pm p^{\uparrow}_\pm)^n, \\ r &= r^{\uparrow\downarrow,L}_\pm + t^{\uparrow,L}_\pm p^{\uparrow}_\pm r^{\uparrow\downarrow,U}_\pm p^{\downarrow}_\pm t^{\downarrow,L}_\pm \sum_{n=0}^{\infty} (r^{\uparrow\downarrow,U}_\pm p^{\downarrow}_\pm r^{\downarrow\uparrow,L}_\pm p^{\uparrow}_\pm)^n. \end{aligned}$$

The first two contributions ($n \leqslant 1$) of the infinite geometric series are shown for transmission and the first ($n = 0$) for reflection. As the surface acts as a planar grating, we can use the previous results of Ref. 31 that report a special case of our more general treatment: $r^{\uparrow\downarrow}_+ = r^{\uparrow\downarrow}_-$, $r^{\downarrow\uparrow}_+ = r^{\downarrow\uparrow}_-$, and $t^{\downarrow}_\pm = t^{\uparrow}_\mp$ can be used. Hence $\mathrm{OA}_R = 0$, but there is no general restriction on OA_T, because the number of passes through the structure is even for reflectivity and each contribution to the sum and hence t on the lower interface and p come only in pairs so that $t^{\downarrow,L}_+ t^{\uparrow,L}_+ = t^{\downarrow,L}_- t^{\uparrow,L}_-$ and $p^{\uparrow}_+ p^{\downarrow}_+ = p^{\uparrow}_- p^{\downarrow}_-$ because of time-inversion symmetry (see Fig. 10).

The phase shift at the surfaces caused by the respective scattering amplitudes is usually negligible for frequencies in the fundamental bands and therefore optical activity is essentially due to the difference in the wave vectors of both eigenmodes (cf. Fig. 10). This straightforward interpretation yields easy and fast numerical analysis of OA that is comparable in magnitude to that of planar, metallic metamaterials[16] and therefore makes the frequency region below the fundamental band edges ($0.5 \lessapprox \Omega \lessapprox 0.6$ in Fig. 9) particularly

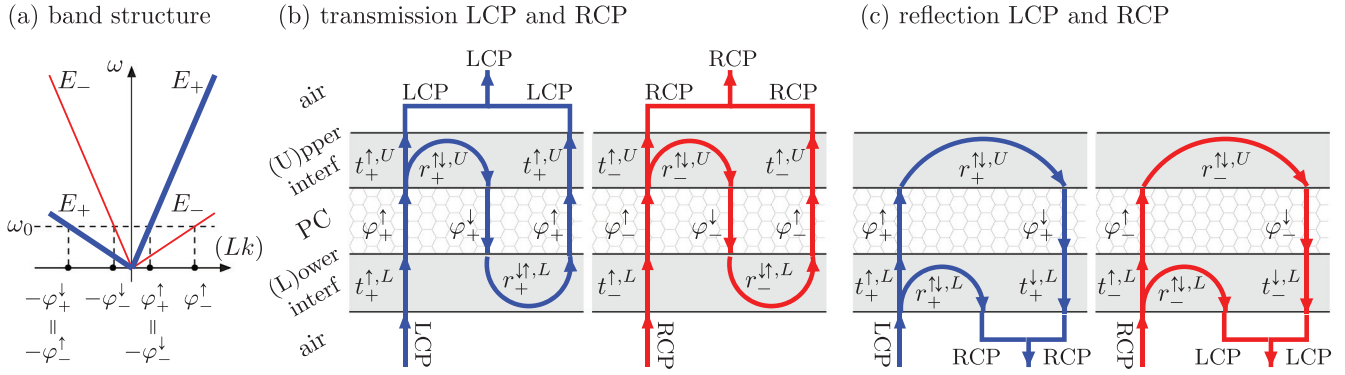

FIG. 10. (Color online) Diagrammatic representation of the processes that lead to different circular-polarization properties of reflected and transmitted light. Assuming that there is a single propagating mode in each channel and direction (a) at a given frequency ω_0, transmission (b) and reflection (c) can be understood by considering positive, upwards pointing k ($\uparrow$) and their counterparts for negative k ($\downarrow$). If the modes further have a leading Bragg order in propagation direction (i.e., interference may be neglected) and the thickness of the slab L is an integer multiple of the lattice parameter a, the difference in k between two modes δk corresponds to an optical phase shift $\delta\varphi = \delta k L$ [cf. Eq. (2)]. The regions labeled upper (U) and lower (L) interface represent the interfacial two-dimensional planes between free space and the photonic crystal that are inflated to finite thickness for visualization. The sign and coloration represents the $E_\pm$ channels in the same manner as in Figs. 4, 8, 5, and 9.

interesting for engineering of optical devices such as beam splitters based on the **8-srs** or similar structures with O point symmetry.

D. No CD in transmission below a critical frequency

For the transmission matrices we derive analogously $\underline{\underline{S}}^{(+)}_{21} = \underline{\underline{S}}^{(-)}_{12}$. This statement is however of less practical relevance because it identifies transmission in the E_+ channel where the source is on one side of the structure with transmission in the E_- channel with the source on the other side and hence corresponds to two distinct experiments. Comparing transmission matrices for the same experiment, we derive from the diagonal entries of the unitarity condition in both channels and the identity of the reflection matrices that the norm of transmission $\underline{\underline{T}}^\dagger\underline{\underline{T}}$ is the same in both channels. Therefore, CD_T is zero below the critical frequency $\Omega_c = 1$ above which energy is able to leak into the (10) Bragg order and hence energy conservation within the (00) order with $\underline{k}$ perpendicular to the plane of interface is not valid. There is no restriction on OA_T that can be finite for all frequencies (see Fig. 9).

Particularly interesting is the magnified region labeled iv in Fig. 5. Transmission is governed by the respective calculated mode of the fundamental band in each channel so that the situation well fits the one illustrated in Fig. 10. If we further assume that the interfacial reflections are sufficiently small (which is expected as transmission is almost 100% in the fundamental bands; see Fig. 9), optical activity is given by $\delta\varphi = \delta k L$ which is estimated to be around 10% at $\Omega \times n_{\mathrm{eff}} = 0.88$.

V. CONCLUSIONS AND OUTLOOK

We have provided consistent analytical and numerical results that demonstrate the potential of the **8-srs** geometry as a dielectric photonic material that should be realizable by current nanofabrication technology. Analytic results, based on versatile group theory and scattering matrix treatment and applicable to any photonic crystal with $I432$ symmetry, are obtained for transmission and reflection amplitudes, and for the topology of the band structure. For the **8-srs** PC, these results are in perfect agreement with numerical simulations that further demonstrate that the **8-srs** exhibits strong optical activity in transmission, comparable to metallic metamaterials, yet without losses and without any ellipticity.

The potential of the **8-srs** for applications as an optically active nanofabricated material, say for the relevant communication wavelength of $\lambda \approx 1.5\ \mu$m, can be gauged from the following considerations. First, if robustness of the optical activity with respect to slight changes in λ is desirable, the data in Fig. 9 suggest a realization of the **8-srs** with a lattice parameter $a = 0.55\lambda \approx 0.83\ \mu$m such that $\omega a/(2\pi c) = a/\lambda \approx 0.55$; the rotation of the polarization plane through a layer of four unit cells (of total thickness 3.5 μm) would then correspond to approximately -8° and close to 100% transmission for both RCP and LCP light and with zero ellipticity, assuming the same values for ϕ and ϵ as in Fig. 9. Second, if a strong dependence of OA on the value of the frequency is acceptable, or even desired, a realization of the **8-srs** with $a = 1.44\ \mu$m, corresponding to $\omega a/(2\pi c) \approx 0.95$, gives a very strong optical rotation of $\approx 50^\circ$, in the optical communication window, again with close to 100% transmission for both RCP and LCP light and with zero ellipticity.

Importantly, Fig. 6 suggests that the parameters chosen here (corresponding to the cross on the white line in Fig. 6) are not optimized to give the strongest photonic response. Specifically, the inverse structure, consisting of hollow air channels along the edges of the **8-srs** structure embedded in a dielectric matrix, has a wider band gap. While the $E_\pm$ frequency split that is desired for many applications is generally stronger for the original **8-srs** structure (cf. higher order bands in Figs. 4 and 5) due to the light-guiding topology of the networks, it is found to be relatively weak in the fundamental bands here as those cross close to the band edge (Fig. 4).

These values for the degree of optical activity should be compared to those in other systems. For quartz, the rotary power varies from 3.2°/mm at wavelength 1.42 μm to 776°/mm at 152 nm,[89] for the liquid crystalline $BP_{SmA}1$ blue phase between 0 and ≈250°/mm over the visible spectral range;[4] for a smectic phase SmC_AP_A a value of 100°–1000°/mm has been reported.[90] For a quasiplanar "twisted-cross" gold metamaterial of thickness 87 nm, Decker *et al*. have reported "strong" rotations of the polarization plane of up to 4°, yet with significant losses;[16] for the split-ring-resonator metamaterial of thickness 205 nm, "huge" rotations of up to 30° are observed with different transmittances for RCP and LCP light of less than 50% (see Fig. 3 in Ref. 91). Song *et al*. have reported even "more gigantic" polarization rotation in a microwave experiment using a chiral composite material, yet also with the losses typical for metallic metamaterials. Note that the dependence on sample thickness (that can be varied in the **8-srs** by varying the number N_z of unit cells) is nonlinear, making a comparison of polarization rotation normalized to the sample thickness less meaningful.

Even for the likely nonoptimal parameters chosen here, the lossless dielectric **8-srs** photonic crystal hence has a significant degree of optical activity, that is combined with the complete absence of ellipticity, absence of losses, and transmission rates of close to 100%. Further, for applications such as beamsplitters where optical properties in various transmission directions are important, the cubic symmetry of the **8-srs** structure is a further benefit to the uniaxial designs of the quasiplanar metamaterials. Given that a single **srs** net with $a_0 = 2a = 1.2$ μm has been realized,[15] it appears likely that future advances in direct laser writing technology make a realization of the **8-srs** or its inverse structure with a lattice size $a = 1$ μm a genuine possibility. Taking all of these considerations into account, we believe that the **8-srs** is a design for a chiral-optical material that is worth further investigation.

Evidently, the validity of all theoretic predictions of this article is not limited to the **8-srs** geometry, but applies more generally to all geometries with symmetry $I432$. It is therefore worth exploring structural databases for other designs with that symmetry; this may include network structures such as the **fcd** net,[92] sphere packings such as Fischer's **4/4/c14** or **3/4/c3** packings,[93] minimal surface geometries such as Koch's $NO3^2$-$c2$ structure,[94] rod packings such as **utz-b**,[95] or woven filaments such as the $P_{129RL}(\cosh^{-1}(3/2))$ structure of Evans *et al*. (see Fig. 8 of Ref. 96).

Beyond the specific symmetry group $I432$, our group theoretic arguments can be adapted to apply more widely to other crystalline chiral materials. For example, the suppression of polarization conversion is expected to be valid for any chiral structure that has m-fold rotations (as opposed to screw rotations) with $m \geqslant 3$ along the [100] propagation direction. These conditions are for example met for all cubic structures with symmetry groups $I432$ (No. 211), $F432$ (No. 209), and $P432$ (No. 207); therefore other network structures with these symmetries may be alternative photonic designs with similar properties. From a perspective of photonic materials, particularly structures with simple cubic P symmetries may be attractive, because of their robustness with respect to the incident wave vector angle; for transmission along the [100] direction of a simple cubic crystal, the X point of the Brillouin zone represents the center of a facet, in contrast to the H point which represents a vertex of the BCC Brillouin zone. Therefore, a small variation in the incident angle will, to first order, not affect the distance between Γ and X in the SC case, again in contrast to the distance between Γ and H in the BCC case. As is the case for the $I432$ symmetry, advanced geometry and structural databases can provide suitable structure candidates, such as **dgn** or **fce**[97] or $P_{118RL}(\cosh^{-1}(\sqrt{6}))$ (see Fig. 14 of Ref. 96).

In a broader context, our study of the **8-srs** geometry demonstrates the benefit of using advanced unconventional concepts of modern real-space geometry, such as the maximally symmetric intergrowth of multiple minimal nets, for the informed design process of functional photonic materials. While numerical photonic methods for transmission parameters and band structures clearly are indispensable tools to translate geometric structure into photonic properties, we have here demonstrated the ability of group theory to provide a firm theoretical understanding of the relationship between photonic functionality and geometric properties for complex three-dimensional chiral photonic crystals.

ACKNOWLEDGMENTS

We are grateful to Stephen Hyde for the inspiration to investigate multiple entangled **srs** nets. We thank Michael Fischer for comments on the manuscript. M.S., K.M., and G.S.T. gratefully acknowledge financial support by the German Science Foundation through the excellence cluster "Engineering of Advanced Materials" at the Friedrich Alexander University Erlangen-Nürnberg. M.S. is grateful to Nadav Gutman for inspiration and the suggestion of group theory as an approach to analyze symmetry behavior. M.T. and M.G. are grateful for financial support by the Australian Research Council through the "Centre for Ultrahigh-Bandwidth Devices for Optical Systems."

APPENDIX A: PROOF THAT POINT SYMMETRY OPERATORS COMMUTE WITH THE MAXWELL OPERATOR

We define the action of the operator $\hat{R}$ on a vector field by $\hat{R}\underline{F}(\underline{r}) = \underline{\underline{R}}\ \underline{F}(\underline{\underline{R}}^{-1}\underline{r})$. The matrices $\underline{\underline{R}}$ are here the common 3×3 matrices that transform three-dimensional vectors according to a point symmetry R, for example given by the Rodriguez formula in the case of a rotation. In the O group these matrices are a suitable choice for the irreducible representation T_1 (Table I). The skew can be understood in terms of an active transformation acting on the vector field itself whereas the change of its position is achieved by a passive transformation that changes space itself. With that definition it is trivial that $\hat{R}\frac{1}{\varepsilon(\underline{r})}\underline{F}(\underline{r}) = \frac{1}{\varepsilon(\underline{r})}\hat{R}\underline{F}(\underline{r})$ for any dielectric function that is invariant under $\hat{R}$ so that we are left to show that $\hat{R}$ commutes with the cross products in the wave equation. The proof is done in a Cartesian basis with

Einstein convention and the abbreviation $\underline{r}' = \underline{\underline{R}}^{-1}\underline{r}$:[101]

$$
\begin{aligned}
[(\imath\underline{k}+\underline{\nabla})\times\hat{R}\underline{u}(\underline{r})]_i &= \varepsilon_{ijk}\left(\imath k_j+\frac{\partial}{\partial x_j}\right)R_{kl}u_l(\underline{r}')\\
&= \varepsilon_{ijk}R_{kl}\left(\imath k_j+\underbrace{\frac{\partial x_m'}{\partial x_j}}_{\overset{(a)}{=}R_{jm}}\frac{\partial}{\partial x_m'}\right)u_l(\underline{r}')\\
&\overset{(a)}{=} \varepsilon_{ojk}R_{op}R_{ip}R_{kl}R_{jm}\\
&\quad\times\left(\imath R_{qm}k_q+\frac{\partial}{\partial x_m'}\right)u_l(\underline{r}')\\
&\overset{(b)}{=} \pm R_{ip}\varepsilon_{pml}\left(\imath(k_m-G_m)+\frac{\partial}{\partial x_m'}\right)u_l(\underline{r}')\\
&= \pm[\underline{\underline{R}}\{(\imath(\underline{k}-\underline{G})+\underline{\nabla})\times\underline{u}\}]_i(\underline{r}')\\
&= \pm[\hat{R}\{(\imath(\underline{k}-\underline{G})+\underline{\nabla})\times\underline{u}(\underline{r})\}]_i.
\end{aligned}
$$

Here we make use of the facts that (a) point symmetries are length preserving and hence the matrix representation is orthogonal, i.e., $R_{ij}R_{kj}=\delta_{ik}$ with the Kronecker symbol δ_{ij}, and that (b) the Levi-Civita symbol ε_{ijk} is invariant under proper [$\det(\underline{\underline{R}})=1$] rotations $\hat{R}^{(+)}$ and changes its sign under improper [$\det(\underline{\underline{R}})=-1$] rotations $\hat{R}^{(-)}$, i.e., $R^{(\pm)}_{il}R^{(\pm)}_{jm}R^{(\pm)}_{kn}\varepsilon_{lmn}=\pm\varepsilon_{ijk}$. The identity in (b) is evident through expansion of the Levi-Civita tensor into a triple product of Cartesian basis vectors (so that $\underline{\underline{R}}$ takes a basic form) and making use of (a).

The change of sign for improper rotations cancels out by the double cross product in the $\hat{\vartheta}_{\underline{k}}$ so that

$$
\begin{aligned}
\hat{\vartheta}_{\underline{k}}\hat{R}\,\underline{u}_{\underline{k},n}(\underline{r}) &= (\imath\underline{k}+\underline{\nabla})\times\left[\frac{1}{\varepsilon(\underline{r})}(\imath\underline{k}+\underline{\nabla})\times\hat{R}\,\underline{u}_{\underline{k},n}(\underline{r})\right]\\
&= \hat{R}\left\{(\imath\underline{k}'+\underline{\nabla})\times\left[\frac{1}{\varepsilon(\underline{r})}(\imath\underline{k}'+\underline{\nabla})\times\underline{u}_{\underline{k}',n}(\underline{r})\right]\right\}\\
&= \hat{R}\,\frac{\omega^2_{\underline{k}',n}}{c^2}\underline{u}_{\underline{k}',n}(\underline{r}) = \hat{R}\,\frac{\omega^2_{\underline{k},n}}{c^2}\underline{u}_{\underline{k},n}(\underline{r})\\
&= \hat{R}\,\hat{\vartheta}_{\underline{k}}\,\underline{u}_{\underline{k},n}(\underline{r}),
\end{aligned}
$$

where we substitute $\underline{k}'=\underline{k}-\underline{G}$ and use the invariance of the periodic Bloch function $\underline{u}_{\underline{k}+\underline{G}}=\underline{u}_{\underline{k}}$ and the eigenfrequencies $\omega_{\underline{k},n}=\omega_{(\underline{k}+\underline{G}),n}$.

APPENDIX B: INCOMPATIBILITY OF CUBIC SYMMETRY AND FFT-BASED ALGORITHMS IN A BCC OR FCC LATTICE

This Appendix discusses the general problem, applicable to all methods based on a three-dimensional fast Fourier transform (FFT) and including the MPB package,[100] that a BCC FFT grid is not compatible with all cubic symmetries. This error is caused by the fact that a BCC fast Fourier grid by definition is incompatible with the full O symmetry (illustrated in Fig. 11) and only has the D_3 point symmetry of the parallelepiped spanned by the three (reciprocal) lattice vectors.

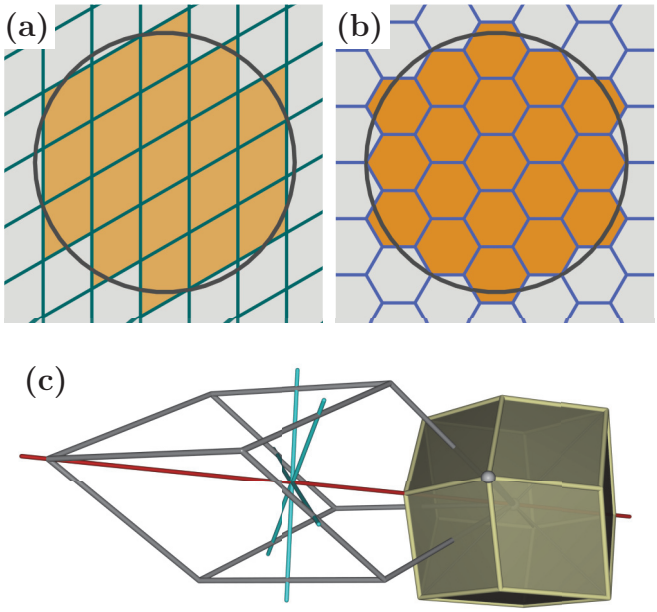

FIG. 11. (Color online) Incompatibility of planar hexagonal and spatial BCC symmetry with the discrete Fourier grid used in PBS plane-wave-based frequency domain eigensolvers. For any planar object with hexagonal symmetry, a discretized representation using a fast Fourier grid that takes exactly two linearly independent basis vectors cannot maintain the full hexagonal symmetry, as (a) illustrates for a circle; a discretization by hexagons (reduced Wigner-Seitz cells), as shown in (b), would alleviate this problem but cannot be implemented for the Fourier analysis. (c) The BCC case represents a 3D analogon with the same problem. The Brillouin zone (solid cell) is a rhombic dodecahedron with full O symmetry, yet the parallelepiped formed by the basis vectors of the Fourier grid representation (hollow cell) only maintains D_3 symmetry with a single 3-fold axis (red) and three 2-fold axes (cyan).

We have identified this general problem as a by-product of our exact group theoretic results for the topology of the band structure—for the band structure of structures with BCC and also hexagonal and face-centered-cubic (FCC) symmetry and possibly others. The BCC Fourier grid can never maintain the full point symmetry (Fig. 11), and hence discretization artifacts are unavoidable and, as Fig. 5 shows, significant even for relatively large sizes of the Fourier grid. We note again that this is an intricacy that is not specific to our application or even to optics and needs to be considered for any numerical algorithm using a three-dimensional FFT on a structure that has BCC, FCC, or hexagonal translational symmetry.

To overcome the symmetry mismatch, in the BCC (FCC) case a simple cubic grid can be used at the price of an increase in numerical grid size by a factor of 2 (4) to obtain equivalent spatial resolution. Figure 5 demonstrates that using a simple (primitive) cubic setup is rectified under certain circumstances where the gain in accuracy through symmetry match is more important than the loss of geometrical detail. A similar approach is not possible for hexagonal lattices where an FFT grid that maintains the 6-fold rotation does not exist.

Here, also FDTD simulations (or any other algorithm working with on a cubic grid) fail to cover the full symmetry of the problem. Not affected are however methods on irregular grids such as finite-element-based calculations that do not yield systematic errors of this kind.

A zoom into the band structure in Fig. 4 reveals (a) that bands do not cross on Δ but are anticrossing correlated with an interchange of characters which is visible in the inset in Fig. 4 where the band structure around the point (0.65, 0.68) is magnified[102] and (b) that the 3-fold degeneracies at the high-symmetry points are slightly lifted (Fig. 5). Both phenomena can be explained with a degenerate perturbation theory model that in case (a) includes only two modes of different representation. The diagonal matrix is perturbed by numerical breaking of the 4-fold symmetry. Case (a) can be treated analytically with the help of direct product selection rules. The perturbation matrix is orthogonal to the A representation and hence the perturbation matrix does not have diagonal elements. It is however still Hermitian so that diagonalization results in a repulsive *force* between two closely spaced bands. Any crossing becomes an anticrossing. The modes mix in equal proportions (and with a phase factor given by the argument of the secondary diagonal entries of the perturbation matrix) at the point of degenerate frequency without perturbation. The modes regain their original character when leaving the degeneracy which can be observed in the inset of Fig. 4 at coordinates (0.65,0.68) where the color is gray at the crossing points and changes to the original E_- (B) color when leaving the degeneracy and also in the fundamental bands at (0.95,0.62).[103] With representation theorem (iii) we can further explain why in case (b) the 3-fold degenerate modes T_1 and T_2 split into a 2-fold and a nondegenerate state as illustrated in Fig. 5 "iiz" and why the E mode does not split up under the symmetry break. The character table for the D_3 point group (cf. Fig. 11) is

D_3	$\mathbb{1}$	$2C_3$	$3C_2'$
$\chi_{A_1}(R)$	1	1	1
$\chi_{A_2}(R)$	1	1	-1
$\chi_E(R)$	2	-1	0

so that we derive

$\mathcal{R}(O)$	A_1	A_2	E	T_1	T_2
$\mathcal{R}(D_3)$	A_1	A_2	E	$A_2 + E$	$A_1 + E$

Note that the reduction of the T_1 representation in C_4 includes a trivial behavior A whereas the reduction of T_2 includes a trivial behavior A_1 in D_3. The black and blue colors of the bands in Fig. 5 "iiz, BCC" are not unique, indicating that the irreducible representation of C_4 is not uniquely determined due to the fact that no symmetry except the identity transformation of C_4 is a symmetry of the discretization and hence the cannot be perfectly met by the numerics.

All modes have the same irreducible representation in the trivial group of the wave vector $S_{\underline{k}} = \mathbb{1}$ on Δ. Modes of same irreducible representation cannot cross each other; they are exposed to a "fermionic" repulsion.[104] That is the reason why the upper two bands in Fig. 5 "ii, BCC" cannot cross each other. Another palpable example for a symmetry-induced "fermionic" anticrossing that is expected for the C_4 symmetry itself and henceforth not related to a numerical symmetry brake is provided by Fig. 5 "i, SC".

*matthias.saba@fau.de
†gerd.schroeder-turk@fau.de

[1] W. C. Johnson, Proteins: Struct., Funct., Bioinf. **7**, 205 (1990).
[2] L. Barron, *Molecular Light Scattering and Optical Activity* (Cambridge University Press, New York, 2009).
[3] M. Schadt and W. Helfrich, Appl. Phys. Lett. **18**, 127 (1971).
[4] E. Grelet, P. J. Collings, M.-H. Li, and H.-T. Nguyen, Eur. Phys. J. E **6**, 157 (2001).
[5] D. Bensimon, E. Domany, and S. Shtrikman, Phys. Rev. A **28**, 427 (1983).
[6] A. Michelson, Philos. Mag. Ser. 6 **21**, 554 (1911).
[7] S. A. Jewell, P. Vukusic, and N. W. Roberts, New J. Phys. **9**, 99 (2007).
[8] V. Sharma, M. Crne, J. Park, and M. Srinivasarao, Science **325**, 449 (2009).
[9] S. Kleinlogel and A. G. White, PLoS One **3**, e2190 (2008).
[10] T.-H. Chiou, S. Kleinlogel, T. Cronin, R. Caldwell, B. Loeffler, A. Siddiqi, A. Goldizen, and J. Marshall, Curr. Biol. **18**, 429 (2008).
[11] M. Saba, M. Thiel, M. D. Turner, S. T. Hyde, M. Gu, K. Grosse-Brauckmann, D. N. Neshev, K. Mecke, and G. E. Schröder-Turk, Phys. Rev. Lett. **106**, 103902 (2011).
[12] S. Vignolini, P. J. Rudall, A. V. Rowland, A. Reed, E. Moyroud, R. B. Faden, J. J. Baumberg, B. J. Glover, and U. Steiner, Proc. Natl. Acad. Sci. U.S.A. **109**, 15712 (2012).
[13] M. Thiel, M. Rill, G. von Freymann, and M. Wegener, Adv. Mater. **21**, 4680 (2009).
[14] M. D. Turner, G. E. Schröder-Turk, and M. Gu, Opt. Express **19**, 10001 (2011).
[15] M. Turner, M. Saba, Q. Zhang, B. Cumming, G. Schröder-Turk, and M. Gu, Nat. Photonics **7**, 801 (2013).
[16] M. Decker, M. Ruther, C. E. Kriegler, J. Zhou, C. M. Soukoulis, S. Linden, and M. Wegener, Opt. Lett. **34**, 2501 (2009).
[17] J. Gansel, M. Thiel, M. Rill, M. Decker, K. Bade, V. Saile, G. von Freymann, S. Linden, and M. Wegener, Science **325**, 1513 (2009).
[18] M. Kuwata-Gonokami, N. Saito, Y. Ino, M. Kauranen, K. Jefimovs, T. Vallius, J. Turunen, and Y. Svirko, Phys. Rev. Lett. **95**, 227401 (2005).
[19] M. Decker, M. W. Klein, M. Wegener, and S. Linden, Opt. Lett. **32**, 856 (2007).
[20] S. Zhang, Y.-S. Park, J. Li, X. Lu, W. Zhang, and X. Zhang, Phys. Rev. Lett. **102**, 023901 (2009); E. Plum, J. Zhou, J. Dong, V. A. Fedotov, T. Koschny, C. M. Soukoulis, and N. I. Zheludev, Phys. Rev. B **79**, 035407 (2009).

[21]J. Pendry, Science **306**, 1353 (2004).
[22]M. Liu, T. Zentgraf, Y. Liu, G. Bartal, and X. Zhang, Nat. Nanotechnol. **5**, 570 (2010).
[23]Shuang Zhang, Jiangfeng Zhou, Yong-Shik Park, Junsuk Rho, Ranjan Singh, Sunghyun Nam, Abul K. Azad, Hou-Tong Chen, Xiaobo Yin, Antoinette J. Taylor, and Xiang Zhang, Nat. Commun. **3**, 942 (2012).
[24]M. Ren, E. Plum, J. Xu, and N. I. Zheludev, Nat. Commun. **3**, 833 (2012).
[25]M. Schäferling, D. Dregely, M. Hentschel, and H. Giessen, Phys. Rev. X **2**, 031010 (2012).
[26]T. Hahn (ed.), *International Tables for Crystallography* (Kluwer Academic Publishers, Dordrecht, 1992).
[27]N. Breova, K. Nakanishi, and R. Woody, *Circular Dichroism: Principles and Applications* (Wiley, New York, USA, 2000).
[28]E. Hecht, *Optics* (Addison-Wesley, Boston, USA, 1998).
[29]J. Joannopoulos, S. Johnson, J. Winn, and R. Meade, *Photonic Crystals: Molding the Flow of Light* (Princeton University Press, Princeton, 2008).
[30]J. Kaschke, J. K. Gansel, and M. Wegener, Opt. Express **20**, 26012 (2012).
[31]B. Bai, Y. Svirko, J. Turunen, and T. Vallius, Phys. Rev. A **76**, 023811 (2007).
[32]B. Bai, K. Ventola, J. Tervo, and Y. Zhang, Phys. Rev. A **85**, 053808 (2012).
[33]C. Menzel, C. Rockstuhl, and F. Lederer, Phys. Rev. A **82**, 053811 (2010).
[34]C. Rockstuhl, C. Menzel, T. Paul, and F. Lederer, Phys. Rev. B **79**, 035321 (2009).
[35]S. I. Maslovski, D. K. Morits, and S. A. Tretyakov, J. Opt. A: Pure Appl. Opt. **11**, 074004 (2009).
[36]V. Dmitriev, Metamaterials **5**, 141 (2011).
[37]V. Dmitriev, IEEE Trans. Antennas Propag. **61**, 185 (2013).
[38]D.-H. Kwon, P. L. Werner, and D. H. Werner, Opt. Express **16**, 11802 (2008).
[39]M. S. Dresselhaus, *Group Theory: Application to the Physics of Condensed Matter* (Springer-Verlag, Berlin and Heidelberg, Germany, 2008).
[40]K. Sakoda, *Optical Properties of Photonic Crystals* (Springer-Verlag, Berlin and Heidelberg, Germany, 2005).
[41]S. T. Hyde, M. O'Keeffe, and D. M. Proserpio, Angew. Chem. Int. Ed. **47**, 7996 (2008).
[42]The network's single type of 3-coordinated vertices is at Wyckhoff sites 8a (.32) in $I4_132$ (No. 214 in Ref. 26).
[43]L. Lu, L. Fu, J. D. Joannopoulos, and M. Soljačić, Nat. Photonics **7**, 294 (2013).
[44]S. S. Oh, A. Demetriadou, S. Wuestner, and O. Hess, Adv. Mater. **25**, 612 (2013).
[45]K. Hur, Y. Francescato, V. Giannini, S. A. Maier, R. G. Hennig, and U. Wiesner, Angew. Chem. Int. Ed. **50**, 11985 (2011).
[46]K. Michielsen and D. Stavenga, J. R. Soc., Interface **5**, 85 (2008); V. Saranathan, C. Osuji, S. Mochrie, H. Noh, S. Narayanan, A. Sandy, E. Dufresne, and R. Prum, Proc. Natl. Acad. Sci. U.S.A. **107**, 11676 (2010); G. Schröder-Turk, S. Wickham, H. Averdunk, M. Large, L. Poladian, F. Brink, J. Fitz Gerald, and S. T. Hyde, J. Struct. Biol. **174**, 290 (2011).
[47]S. Vignolini, N. A. Yufa, P. S. Cunha, S. Guldin, I. Rushkin, M. Stefik, K. Hur, U. Wiesner, J. J. Baumberg, and U. Steiner, Adv. Mater. **24**, OP23 (2011).
[48]C. Mille, E. C. Tyrode, and R. W. Corkery, RSC Adv. **3**, 3109 (2013); Chem. Commun. **47**, 9873 (2011).
[49]C. Pouya and P. Vukusic, Interface Focus **2**, 645 (2012).
[50]S. T. Hyde and S. Ramsden, Europhys. Lett. **50**, 135 (2000).
[51]S. T. Hyde and C. Oguey, Eur. Phys. J. B **16**, 613 (2000).
[52]M. E. Evans, V. Robins, and S. T. Hyde, Acta Crystallogr., Sect. A **69**, 241 (2013).
[53]The BCC Wigner-Seitz cell forms a Kelvin body that is a cube truncated along its [100] directions to give a polytope with 14 facets, eight of which are regular hexagons and six of which are squares, also known as truncated octahedron. The use of the term *Kelvin body* for this cell is motivated by it being Kelvin's proposition for the cell with least surface area (given fixed volume) that can tessellate space (Ref. 98).
[54]See also the reticular chemistry structure resource http://www.rcsr.anu.edu.au (Ref. 97) for details, where the 2-**srs**, the 4-**srs**, and the 8-**srs** are denoted srs-c2*, srs-c4, and srs-c8, respectively.
[55]Y. Han, D. Zhang, L. Chng, J. Sun, L. Zhao, X. Zou, and J. Ying, Nat. Chem. **1**, 123 (2009).
[56]S. T. Hyde, L. Di Campo, and C. Oguey, Soft Matter **5**, 2782 (2009).
[57]J. J. K. Kirkensgaard, Phys. Rev. E **85**, 031802 (2012).
[58]G. E. Schroder-Turk, L. de Campo, M. E. Evans, M. Saba, S. C. Kapfer, T. Varslot, K. Grosse-Brauckmann, S. Ramsden, and S. T. Hyde, Faraday Discuss. **161**, 215 (2013).
[59]B. P. Cumming, M. D. Turner, S. Debbarma, B. Luther-Davies, G. Schröder-Turk, and M. Gu, in *Frontiers in Optics Conference* (Optical Society of America, New York, USA, 2012), p. FW1F.7.
[60]The upper T_1 mode is out of frequency boundaries in Fig. 4.
[61]These include previous results (Refs. 30, 31, and 33) as special cases.
[62]Note that for compactness of notation we suppress that α itself depends on i; i.e., $\alpha = \alpha_i$.
[63]The procedure for the electric field equation is analogous. We note, however, that the character of any improper rotation of the E field is the negative of the H-field character which can be seen for example by using Faraday's equation. While any $I432$ PC does not exhibit any improper rotation, any dielectric PC has time-inversion symmetry that is *improper* and hence induces the same phase shift between H and E field.
[64]This defines a set of all propagating modes in a semi-infinite structure. However, for any real scattering problem a complete set of PC modes includes evanescent modes. The impact of evanescent waves onto the scattering process becomes dominant if there is no propagating mode present in the transmission channel that has a finite amount of energy in the 00 Bragg order to which the incident beam couples only. This makes it for example impossible to get any useful information about transmission through a finite slab in the frequency range between $\Omega := \omega a/(2\pi c) = 0.66$ and 0.71 from the band structure in Fig. 4 alone.
[65]Conservation of the spatiotemporal modulation at the surface implies conservation of frequency and parallel part of the wave vector where the PC acts as a grating and back-scattering can occur into several Bragg orders; i.e., back-scattered waves are given by a plane-wave Floquet basis.
[66]Also known as 432 in Hermann-Maugin notation.
[67]Technically, a class is a subset S_n of symmetry elements that is obtained by one selected member and all elements that are conjugate. As a result, for most purposes all elements of a

class can be treated equally; i.e., they have same character, etc.

[68]E. Nicoletti, G. Zhou, B. Jia, M. J. Venture, D. Bulla, B. Luther-Davies, and M. Gu, Opt. Lett. **33**, 2311 (2008).

[69]Transmission simulations are performed with the open-source finite-difference time domain package MEEP (Ref. 99). Simulations are for a slab of 53 unit cells of **8-srs** structure. Periodic boundary conditions are assumed in all three directions of the simulation box with a Yee grid of 64 points per unit cell and a size of $1 \times 1 \times 61$ unit cells. A combination of respectively 2 unit cells *vacuo* and perfectly matched layers on each side are used with a Gaussian source in vacuum on one side and energy flux measured on the other. Band structure frequencies and eigenmodes are calculated with the open-source plane-wave frequency domain eigensolver MPB (Ref. 100) with a 128^3 structural resolution and a 32^3 Fourier grid in the primitive body-centered-cubic basis.

[70]Simulations are performed with the commercial software package CST Microwave Studio. We used the finite-element frequency domain solver with periodic boundary conditions in the transverse plane and a 3 [4] unit cells wide slab of the **8-srs** structure. Perfectly matched layers are used for the z boundaries of the simulation box.

[71]The infinite size in x and y direction is achieved by use of periodic boundary conditions with a single unit cell of the **8-srs** structure.

[72]The termination determines the planes at which the infinite periodic crystal is clipped to give the slab of height $n_z a$. The termination is indicated by the vertical clipping position t in crystallographic coordinates, with $t = 0$ corresponding to a clipping plane through the point with symmetry 432 (the origin in the notation of Ref. 26).

[73]The main Bragg contribution $\underline{G}$ to the SC Bloch mode is determined and the band structure unfolded plotting $1 - k$ and exchanging $E_+ \leftrightarrow E_-$ if $2\pi \underline{G} \cdot \underline{e_k}/a$ yields an odd number.

[74]The sum over α is unnecessary in this special case as all C_4 representations are one-dimensional.

[75]For any dielectric PC as shown in Ref. 29 on page 41f where a simple proof of the Hellmann-Feynman relation is also given if ∇_k is replaced by a general derivative.

[76]This claim can be proved with degenerate perturbation theory. The irreducible representation of the point group of the wave vector is reduced in the lower symmetry group of δk and the matrix elements of the perturbation operator $\hat{\vartheta}_{\delta k}$ in this basis are diagonalized (similar to the $k \cdot p$ analog in quantum mechanics). As all matrix elements satisfy the symmetry relation $\langle \hat{\vartheta}_{-\delta k} \rangle = -\langle \hat{\vartheta}_{\delta k} \rangle$, there is always a band with continuous slope passing through the point without changing its representation. The Γ_0 point where E and H are decoupled and hence the group velocity is zero whereas finite in the vicinity of Γ is an exception.

[77]The term *anticrossing* is taken from Ref. 39 and is used to characterize two bands that come close to each other and seem to interchange group velocities from left to right without actually touching one another.

[78]We have adopted the term degeneracy although the states have opposite Bloch wave vector and generally different representation.

[79]Generally, a third case can occur where neither statement (a) nor (b) holds. However, this case only occurs in the presence of a 4-fold improper rotation or a two-fold screw axis that are both not present and generally cannot be in the group of the wave vector within the Brillouin zone (Ref. 81).

[80]W. Ludwig and C. Falter, *Symmetries in Physics: Group Theory Applied to Physical Problems* (Springer-Verlag, Berlin and Heidelberg, Germany, 1988).

[81]C. Herring, Phys. Rev. **52**, 361 (1937).

[82]Technically, this is a choice of natural basis states where either the magnetic (s) or the electric (p) field lies in the plane of incidence of the respective plane-wave component, i.e., the plane spanned by the wave vector and the surface normal. That definition corresponds to polar coordinate system (r,ϕ,z) with the 4-fold axis as its center so that the polarization state translates as $s = r$ and $p = \phi$. In that local coordinate system, the action of any $R \in C_4$ onto e_σ is the identity transformation. Note that we only use the polar system for the field vectors and not for the position vector so that all spatial derivatives, etc., are still Cartesian.

[83]$R(0,0)^T = (0,0)^T \forall \hat{R} \in C_4$ yields $f^{A,B}_{\sigma,(0,0)^T} = 0$ and $f^{(i)}_{x,(0,0)^T} = f^{(i)}_{y,(0,0)^T}$.

[84]Because the layer is thin, the structure is assumed to be homogeneous along z within that layer; i.e., $\varepsilon(z) = \varepsilon(z + z_0)$ if $|z_0| < \delta/2$.

[85]It can be numerically computed by conversion of the planar Bloch-Maxwell equation into an eigenvalue equation for q_d (Ref. 87).

[86]z-inversion symmetry around the homogeneous layer center and time-inversion symmetry guarantee that in each case states come in pairs $q_\pm$.

[87]D. M. Whittaker and I. S. Culshaw, Phys. Rev. B **60**, 2610 (1999).

[88]The change of sign in the exponential is irrelevant as the basis functions have a symmetry $f_{\sigma,n} = f_{\sigma,-n}$ that is due the vectorial nature of f and $\chi_{E_\pm}(C_2) = -1$ and can be seen acting with $\hat{C}_2$ twice upon f using the explicit form and the representation form each once.

[89]T. Radhakrishnan, Proc. Indian Acad. Sci., Sect. A **25**, 260 (1947).

[90]L. E. Hough, C. Zhu, M. Nakata, N. Chattham, G. Dantlgraber, C. Tschierske, and N. A. Clark, Phys. Rev. Lett. **98**, 037802 (2007).

[91]M. Decker, R. Zhao, C. M. Soukoulis, S. Linden, and M. Wegener, Opt. Lett. **35**, 1593 (2010).

[92]O. Delgado-Friedrichs, M. D. Foster, M. OKeeffe, D. M. Proserpio, M. M. Treacy, and O. M. Yaghi, J. Solid State Chem. **178**, 2533 (2005).

[93]W. Fischer, Acta Crystallogr., Sect. A **60**, 246 (2004).

[94]E. Koch, Acta Crystallogr., Sect. A **56**, 15 (2000).

[95]N. L. Rosi, J. Kim, M. Eddaoudi, B. Chen, M. O'Keeffe, and O. M. Yaghi, J. Am. Chem. Soc. **127**, 1504 (2005).

[96]M. E. Evans, V. Robins, and S. T. Hyde, Acta Crystallogr., Sect. A **69**, 262 (2013).

[97]M. O'Keeffe, M. Peskov, S. Ramsden, and O. Yaghi, Acc. Chem. Res. **41**, 1782 (2008).

[98]W. Thomson, Acta Mathematica **1**, 121 (1888).

[99]A. F. Oskooi, D. Roundy, M. Ibanescu, P. Bermel, J. D. Joannopoulos, and S. G. Johnson, Comput. Phys. Commun. **181**, 687 (2010).

[100]S. Johnson and J. Joannopoulos, Opt. Express **8**, 173 (2001).

[101]An alternative proof is provided in Ref. 40.

[102]The points are all equal sized in the inset and colored by the color of i with dominating N_i with intensity maximum at $N_i = 1$ and continuously decreasing to light gray at $N_i = 0.25$.

[103]The color code of the $E_\pm$ modes in the main plot is in the common hexadecimal rgb scheme defined by $RGB = C\lfloor 255(N_{E_+} - N_{E_-})\rfloor$ where $C = 256^2$ if $N_{E_+} > N_{E_-}$ and $C = 1$ else.

[104]Electromagnetic eigenmodes (unlike photons in a particle picture) behave like fermions: There can only be a single mode in a state classified by all symmetries (or quantum numbers) because the two modes are uniquely determined except for a scalar coefficient and hence interchangeable. The symmetries in Maxwell theory are translation invariance in time and space (ω and k), time inversion ($k \leftrightarrow -k$), and point symmetries (character).